In-depth characterisation of organic matter thermal lability and composition from Arctic Permafrost thaw slumps

Marco A. Bolandini[1], Jordon D. Hemingway[1], Negar Haghipour[1,2], Kirsi H. Keskitalo[4], Jorien E. Vonk[3], Timothy I. Eglinton[1], Lisa Bröder[1]

[1]Geological Institute, Department of Earth and Planetary Sciences, ETH Zurich, Sonneggstrasse 5, 8092 Zurich, Switzerland
[2]Laboratory for Ion Beam Physics, Department of Physics, ETH Zurich, Otto-Stern-Weg 5, 8093 Zurich, Switzerland
[3]Earth and Climate, Faculty of Science, Vrije Universiteit Amsterdam, De Boelelaan 1085, 1081 HV Amsterdam, Netherlands
[4]School of Geography and Natural Sciences, Northumbria University, Ellison Place, Newcastle upon Tyne UK-NE1 8ST, United Kingdom

Correspondence to: Marco A. Bolandini (marcobo@eaps.ethz.ch)

Abstract

The rapid warming of the Arctic is accelerating permafrost thaw and mobilising large, previously frozen organic-carbon reservoirs. Retrogressive thaw slumps (RTS) are dynamic hotspots of abrupt permafrost disturbance that expose deep, millennial-aged material to erosion and transport. To assess the fate of slump-derived organic matter (OM), we analysed samples from (i) the seasonally thawed active layer, (ii) Holocene and Pleistocene permafrost, (iii) freshly thawed debris, and (iv) runoff across four RTS of contrasting sizes and ecological settings on the Peel Plateau, north-western Canada. We specifically quantified OM abundance, thermal stability, and radiocarbon content, complemented by thermally-sliced pyrolysis–gas chromatography–mass spectrometry (Ts-Py-GCMS) for molecular fingerprints. Our results show that OM age and stability primarily reflect geomorphic feature type. Permafrost, debris, and runoff contain radiocarbon-depleted, thermally stable carbon, whereas active-layer OM is younger and more labile, with minor contributions of stabilised, higher-energy fractions. Ts-Py-GCMS shows that low-temperature fractions are dominated by carbohydrate- and cellulose-derived pyrolysates, while higher-temperature fractions contain aromatic and long-chain aliphatic compounds consistent with more processed or mineral-associated OM. The close similarity between permafrost, debris, and runoff indicates that RTS predominantly export ancient, thermally stable OM with limited early-stage alteration. These findings highlight that a substantial portion of thaw-mobilised particulate carbon likely remains stable during initial transport, with important implications for Arctic carbon-climate feedbacks.

1 Introduction

Arctic amplification has led to regional warming rates two to four times the global mean (Overland et al., 2019; Rantanen et al., 2022), thus accelerating permafrost thaw and the release of large, previously frozen organic carbon stocks (Hugelius et al., 2014; Schuur et al., 2015). Soils across the permafrost region store approximately 1,000 Pg C within the upper 3 m (Hugelius et al., 2014; Mishra et al., 2021), representing nearly half of the global below-ground carbon pool. Even partial decomposition of this reservoir could substantially alter global biogeochemical cycles. Thaw and mobilisation heighten the vulnerability of this pool to decomposition, emphasising its potential role in amplifying climate warming (Schuur et al., 2015). Once thawed, some fraction of organic matter (OM) is likely remineralised, thereby leading to carbon dioxide (CO_2) and methane (CH_4) emissions and reinforcing warming (Schuur et al., 2008). However, increased plant productivity ("Arctic greening") has the potential to offset part of these emissions; the net carbon balance of the Arctic under continued warming thus remains uncertain (Strauss et al., 2025).

Retrogressive thaw slumps (RTS) are among the most dynamic features of permafrost degradation. They form when ground-ice melt triggers large-scale collapse of previously frozen deposits, exposing deep, often Pleistocene-aged material to erosion and rapid transport (French, 2007). Each slump is characterised by a steep, ice-rich headwall that retreats upslope as thaw progresses, and a downslope scar zone where thawed sediment accumulates and may be re-mobilised and transported farther downslope (Bröder et al., 2021; French, 2007; Kokelj et al., 2021; Segal et al., 2016a). Compared to gradual thaw, RTS activity strongly enhances particulate organic carbon (POC) and sediment fluxes to downstream systems (Kokelj et al., 2013, 2021; Zolkos et al., 2019). Mobilised OM can also enter river networks as dissolved organic carbon (DOC), which has been described as microbially labile (Drake et al., 2015; Mann et al., 2015; Vonk et al., 2015), while POC lability remains relatively poorly constrained. In incubation experiments, this POC has shown low biodegradability (Kokelj et al., 2021), suggesting persistence after thawing. While incubation experiments provide valuable constraints on microbial respiration in thawed soils, they are usually laborious and time consuming, often underestimate the stability of mineral-associated or physically protected carbon pools and cannot resolve how molecular composition relates to OM reactivity (Lacelle et al., 2019; Shakil et al., 2022). These limitations highlight the need for complementary, process-based approaches that link OM composition to its (thermal) reactivity and radiocarbon age structure, and thus provide mechanistic constraints on the stability and fate of RTS-derived organic carbon.

The Peel Plateau in north-western Canada is one of the most active and rapidly evolving regions of RTS development in the Arctic (Kokelj et al., 2015, 2021; Littlefair et al., 2017). Successive investigations have documented RTS-driven transformations in sediment delivery, stream geomorphology, and carbon export (Kokelj et al., 2013, 2015, 2017, 2021). These studies show that slump activity markedly increases sediment and POC fluxes, largely sourced from ancient, Holocene- and Pleistocene-aged permafrost (Bröder et al., 2021; Kokelj et al., 2021; Shakil et al., 2020; Keskitalo et al., 2021). Active-layer deepening and cryoturbation (i.e., frost-driven mixing of soil horizons and OM) further redistribute carbon vertically within thawing terrains, influencing its exposure and preservation (Bockheim and Tarnocai, 1998; Ping et al., 1998, 2008). Mapping

Deleted: thermal
Deleted: -based
Deleted: ,
Deleted: providing
Deleted: —
Deleted: —

and geomorphic classification efforts have demonstrated that slump morphology controls both the rate and pathway of material transfer to aquatic systems (Kokelj et al., 2013, 2015; Lewkowicz and Way, 2019; Ramage et al., 2017). Prior work on the Peel Plateau has quantified sediment and carbon fluxes and source contributions (Littlefair et al., 2017; Shakil et al., 2020; Zolkos et al., 2018) and has identified geomorphic controls on material export (Kokelj et al., 2013, 2021). Furthermore, Bröder et al. (2021) showed that active-layer material is dominated by compounds indicative of fresh plant material, whereas recently thawed debris and slump runoff predominantly carry radiocarbon-depleted POC, compositionally more similar to permafrost OM. Despite these advances, the overall assessment of bulk OM stability in these RTS systems remain poorly constrained. Specifically, how OM composition relates to its (thermal) reactivity and inferred persistence during downstream transport is not yet understood.

Here, we address these knowledge gaps by providing a mechanistic framework to distinguish stabilised versus degradable carbon fractions and assess the initial fate of slump-derived OM upon thaw and mobilisation. To do so, we collected samples at four RTS sites, spanning from small, tundra-dominated slumps to larger, forested slumps, that differed in headwall height, scar zone extent, initiation age, elevation, and predominant vegetation (Fig. 1), to measure thermal reactivity and thermally resolved radiocarbon content together with molecular composition distributions of OM. Although thermal reactivity does not equate with bioavailability, it provides an indirect measure of OM persistence by constraining its activation energy structure (Hemingway et al., 2017). We focus on four RTS components representing two primary OM sources: the seasonally thawed active layer, and permafrost layers that formed during Holocene and Pleistocene, now exposed at the retreating headwalls; and two stages of mobilisation: freshly thawed debris accumulating at the base of the headwall and suspended sediments in runoff draining the slump scar zone. We can thus test the following hypotheses: (i) permafrost OM contains radiocarbon-depleted yet thermally heterogeneous carbon, comprising components with contrasting activation energies whose preservation reflects prolonged freezing rather than intrinsic molecular resistance. And: (ii) in contrast, the active layer contains younger organic compounds from recent biological production characterised by lower activation energies. Building on this foundation, we propose that activation-energy distributions provide a mechanistic insight into these compositional contrasts, allowing us to assess how OM from contrasting sources transforms upon erosion and transport. This information improves our understanding of how abrupt permafrost thaw and subsequent OM mobilisation influences permafrost carbon cycling and associated climate feedbacks.

Deleted: —
Deleted: —
Deleted: -
Deleted: —
Deleted: —
Deleted: mobilisation:— freshly

2 Material and Methods

2.1 Site description and sample preparation

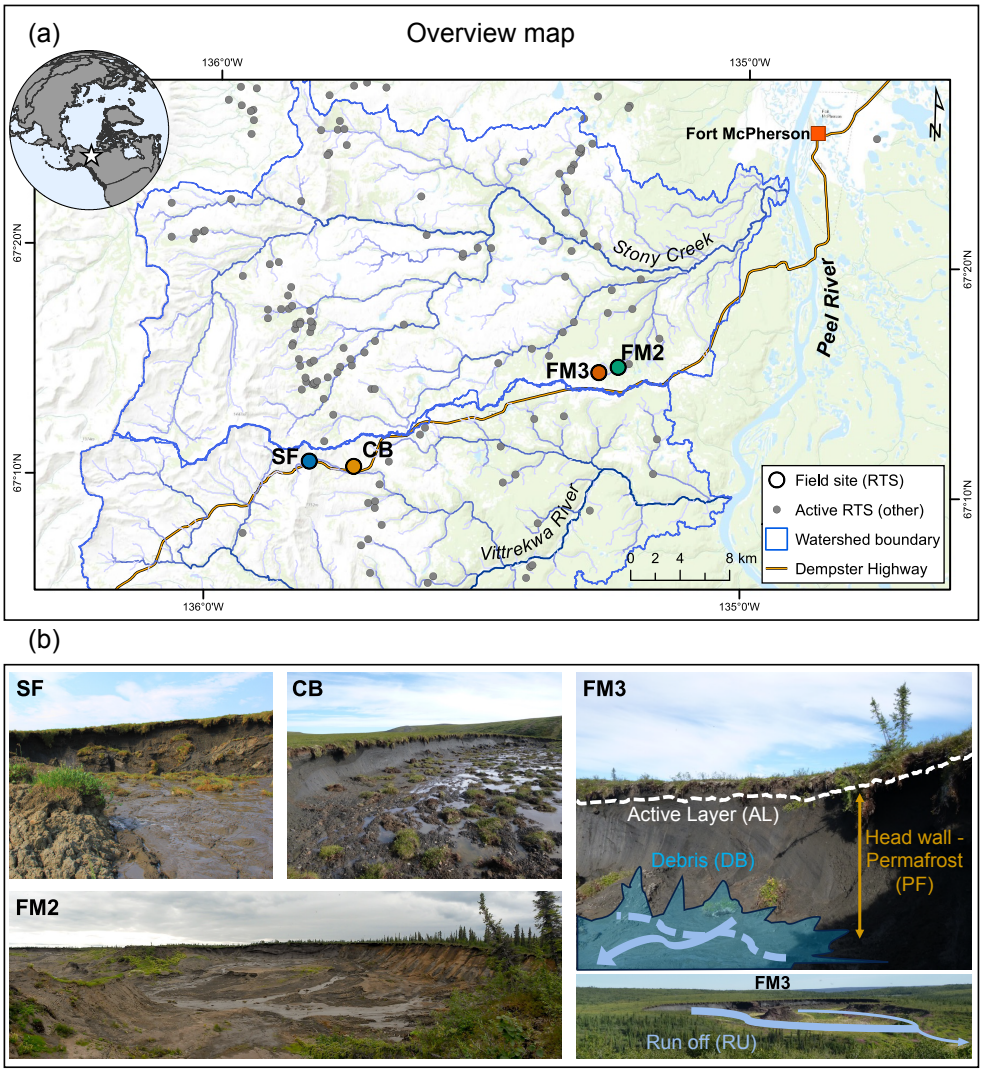

Figure 1. (a) Map of the study area on the Peel Plateau, NWT, Canada (as indicated by the star on the inserted overview map), showing the locations of the four investigated retrogressive thaw slumps (RTS): CB (blue), SF (yellow), FM2 (green) and FM3 (red). The broader distribution of active thaw slumps across the region, mapped using Landsat imagery up to 2015, is shown as grey dots, and the Stony Creek and Vittrekwa River watersheds are outlined in blue. Geospatial data on thaw slump distribution were obtained from Segal et al. (2016). (b) Photographs of each of the RTS features. The photos of FM3 thaw slump illustrate the geomorphological features: active layer (AL – white dotted line), permafrost (PF – orange), debris (DB – blue), and runoff (RU – blue arrow). The figure has been adapted from Bröder et al. (2021) and the basemap is from Zolkos et al. (2018). Reproduced with permission from John Wiley & Sons. ©2018 American Geophysical Union.

The RTS sites studied here (Fig. 1a) have been described in detail previously (Bröder et al., 2021, Keskitalo et al., 2021) and have featured in related work on sediment dynamics and carbon fluxes (Littlefair et al., 2017; Shakil et al., 2020; Thomas et al., 2023; Zolkos et al., 2019). Sites CB and SF are smaller, more recently initiated RTS systems at higher elevation within tundra-like vegetation, whereas sites FM2 and FM3 are older, much larger and at lower elevation in more forested settings (Table 1). Samples were collected from the four key geomorphological features common to each slump: seasonally thawed active layer (AL), Holocene (HO) (and deeper Pleistocene (PL) where exposed) permafrost (PF) layers, freshly thawed slump debris (DB), and suspended sediments in runoff (RU). These zones are illustrated in the images of the FM3 headwall in Fig. 1b.

Table 1: Geomorphic characteristics of the four retrogressive thaw slumps studied. Values are based on field measurements from the 2017 campaign; further site descriptions are provided in Bröder et al. (2021), Segal et al. (2016), and Zolkos et al. (2019).

Site	Coordinates	Elevation (m)	Active-layer depth (cm)	Headwall height (m)	Scar-zone area (ha)
CB	67.182° N, 135.732° W	576	46	5.8	3.4
SF	67.183° N, 135.811° W	720	56	7.6	< 1
FM2	67.257° N, 135.236° W	338	23	24.2	48
FM3	67.253° N, 135.273° W	391	65	9.8	10

Site parameters were measured during the sampling campaign in 2017 and are described in more detail by Bröder et al. (2021) and Zolkos et al. (2019) (Table 1). In short, active-layer material was sampled from the headwall, permafrost blocks were cut directly from exposed headwalls, and debris and runoff sediments were collected with stainless-steel scoops following the procedures outlined in Bröder et al. (2021). Samples were placed in pre-cleaned containers, stored frozen until return to the laboratory, and subsequently freeze-dried, ground, and homogenised prior to analysis. Inorganic carbon was removed by acid fumigation with concentrated hydrochloric acid (HCl) for 72 h at 60 °C, following standard procedures for solid-phase organic-matter analysis (Harris et al., 2001; Komada et al., 2008). Pre-treated samples from all four sites (CB, SF, FM2, FM3)

Deleted: 45–55
Deleted: 5–8
Deleted: < 3
Deleted: 45–55
Deleted: 5–8
Deleted: 3
Deleted: 20–65
Deleted: up to 24
Deleted: 10–48
Deleted: 20–65
Deleted: up to 24
Deleted: 10–48
Deleted: from shallow soil pits
Formatted: Font: (Default) +Body (Times New Roman), 10 pt, Font color: Text 1, English (UK)

were first analysed using solid total organic carbon analysis (SoliTOC) to provide a bulk assessment of OM content and thermal lability (Mittelbach et al., 2025). A subset of samples from the larger slumps (FM2 and FM3) was subsequently investigated by online ramped oxidation-accelerator mass spectrometry (ORO-AMS) and thermally sliced-pyrolysis-gas chromatography mass spectrometry (Ts-Py-GCMS) to determine the radiocarbon age, energy distribution, and molecular composition of thermally resolved fractions.

2.2 Solid Total Organic Carbon analysis (SoliTOC)

SoliTOC analyses were carried out to obtain an overall characterisation of OM thermal stability across the geomorphological features of each thaw slump. For each sample, ~50 mg of pre-treated material was loaded into a ceramic crucible and analysed using a SoliTOC Cube analyser (Elementar GmbH) following the German industrial standard DIN 19539 (Deutsches Institut für Normung, 2016-08). Instrument calibration employed a calcium-carbonate ($CaCO_3$) standard containing 12 % total inorganic carbon (minimum p.A. quality) mixed with aluminium oxide (Al_2O_3). Analytical accuracy was verified using two certified reference materials: a high-organic-carbon sediment (Säntis SA33802151, 7.45 % C) and a low-organic-carbon soil (Säntis SA33802152, 1.54 % C). Precision within the analytical sequence was assessed using repeated analyses (n = 5 for each standard), yielded standard deviations of 0.05 % C and 0.02 % C, corresponding to relative standard deviations of 0.7 % and 1.3 %, respectively. Mean recoveries were 97.35 % (SA33802151) and 99.51 % (SA33802152), confirming stable and accurate instrument performance.

Organic carbon was quantified using three operationally defined temperature steps following DIN 19539: total organic carbon released during the 400 °C isothermal step (TOC_{400}), representing a thermally labile pool; residual oxidisable carbon (ROC), released during the subsequent 600 °C step; and total inorganic carbon (TIC), released during the final 900 °C step. Rapid heating between steps minimises CO_2 release during temperature ramps, such that carbon is operationally assigned to the target isothermal intervals rather than to a continuous temperature ramp (Mittelbach et al., 2025).

The sum of TOC_{400} and ROC was defined as total organic carbon (TOC). Because a small fraction of thermally recalcitrant OC appears to combust within the nominal TIC window, the operational fractions TOC_{400} and ROC should be interpreted strictly as method-defined thermal lability pools. The ROC/TOC ratio, first introduced as an operational index of recalcitrance by Mittelbach et al. (2025), may therefore serve as a proxy for intrinsic oxidation resistance but is not necessarily equivalent to biological lability (see Results and Discussion for an assessment of methodological limitations). For completeness, total carbon (TC), defined as the sum of TOC and TIC, was also reported to verify bulk carbon consistency across analytical methods (Supplementary Table S2).

Deleted: The ROC/TOC ratio therefore may serve as a proxy for intrinsic recalcitrance but is not necessarily identical to biological lability (see Results and Discussion for an assessment of methodological limitations).

2.3 Online ramped oxidation-accelerator mass spectrometry (ORO-AMS)

To resolve the age structure of OM thermal-lability fractions, ORO-AMS analyses were conducted using the setup described by Bolandini et al. (2025). This method captures and measures radiocarbon activity of CO_2 that is released across a series of temperature windows. Briefly, the system features a dual-oven configuration: the first oven (where the sample is loaded) applies a linear temperature ramp to progressively oxidise OM from the sample, while the second oven is maintained at constant temperature and contains catalytic material to ensure complete oxidation and removal of non-carbon species. Released CO_2 within each temperature window is then purified, trapped using a dual trap molecular zeolite interface (De Maria et al., 2021), it is first purified, and transferred to an accelerator mass spectrometer (Low Energy Accelerator, LEA, IonPlus) for radiocarbon measurement (Ramsperger et al., 2024; Synal et al., 2007).

In this study, approximately 40–50 mg of acid-fumigated, homogenised material from each geomorphological feature of the larger thaw slumps (FM2 and FM3) was analysed individually, including replicate combustions of selected samples (10 primary analyses plus 3 replicates). Additional combustions from FM2, FM3, CB, and SF were conducted for pre-screening and bulk characterisation. In total, more than 30 ORO combustions were performed across all sites. Samples were loaded into pre-combusted quartz tubes placed within the oxidation reactor. The ramping furnace was programmed to heat linearly at 5 °C min^{-1} from 150 °C to 900 °C under a continuous flow of 18 % O_2 in He (90 mL min^{-1}). This oxygen-rich carrier gas was used to promote complete oxidative decomposition of the sample and minimise charring during ORO–AMS analysis. The carrier-gas flow of 90 mL min^{-1} was selected based on previous optimisation of the ORO–AMS setup, where this setting provided stable gas transport, limited reflux or back-mixing, and ensured reproducible CO_2 transfer to the trapping interface (Bolandini et al., 2025). A heating rate of 5 °C min^{-1} was used to provide sufficient thermal resolution while maintaining adequate CO_2 yield per temperature interval for AMS analysis. The influence of ramp rate on thermogram shape and activation-energy estimates is explicitly treated in the kinetic framework used here (Hemingway et al., 2017). Nevertheless, because ramp rate, gas composition, flow rate, and system configuration can influence thermogram shape and apparent thermal metrics, comparisons among RPO/ORO studies should consider operational differences, as also noted for other ramped oxidation and thermal–radiocarbon approaches (Dasari and Widory, 2022; Garnett et al., 2023; Stoner et al., 2023).

Radiocarbon analyses were performed on predefined temperature windows (150–240, 240–300, 300–350, 350–400, 400–455, 455–510, and 510–600 °C), selected to provide a consistent temperature framework for comparison with the SoliTOC decomposition scheme. While this alignment facilitates cross-method interpretation, it does not imply direct equivalence of OM fractions, given the differing analytical conditions and reaction pathways involved. For consistency, we also calculated an ORO-based ROC/TOC ratio by integrating CO_2 released between 400 and 600 °C relative to the total CO_2 released below 600 °C. Temperatures above 600 °C were excluded from radiocarbon analysis because CO_2 yields were insufficient to sustain a stable AMS ion current and because our focus was on the sub-600 °C domain that corresponds to the operational ROC threshold used in SoliTOC. However, small amounts of refractory OC may combust above 600 °C in some

Deleted: .¶
Formatted: Font: (Default) Times New Roman
Formatted: Font: (Default) +Body (Times New Roman)
Formatted: Font: (Default) +Body (Times New Roman)
Formatted: Font: (Default) +Body (Times New Roman)
Deleted:
Formatted: Font: (Default) Times New Roman
Deleted: organic matter
Deleted: chosen to align with and extend the decomposition framework established by the SoliTOC analysis.
Deleted: OC

samples (see Results and Discussion for an assessment of methodological limitations). Samples were ramped to 900 °C, but thermograms are displayed only up to 800 °C because only minimal additional CO_2 was released above this temperature.

Evolved CO_2 was continuously monitored and recorded as thermograms (i.e., plots of CO_2 yield as a function of temperature), providing real-time information on OM oxidation behaviour and decomposition kinetics. Gaussian and Savitzky–Golay smoothing were applied to minimise CO_2 and temperature instrumental noise. Radiocarbon results were normalised to Ox-II reference material and corrected for machine and procedural blanks following standard ETH protocols (Synal et al., 2007) and are reported as fraction modern ($F^{14}C$), following the guidelines detailed by Reimer et al. (2004, 2020). Typical analytical uncertainties ranged from ±0.003 to ±0.010 $F^{14}C$ depending on CO_2 yield (Stuiver and Polach, 1977). For quality control, bulk-equivalent $F^{14}C$ was reconstructed as the CO_2-weighted mean of $F^{14}C$ results for each ORO-AMS thermal window and compared to previously published bulk radiocarbon measurements (Supplementary Discussion Table S1, Fig. S1, Table S3 from Bröder et al., 2021).

Subsequent data analysis integrating CO_2 thermograms with $F^{14}C$ results was performed using the open-source Python package "rampedpyrox" (Hemingway, 2016). Interpretation followed the mechanistic framework of Hemingway et al. (2017, 2019), which links decomposition profiles to underlying distributions of OM activation energy, E. These distributions, termed $p(0, E)$, represent the resistance of OM to oxidative decomposition and thus provide an integrated measure of OM reactivity governed by molecular composition and stabilisation mechanisms. To further compare $p(0, E)$ distributions across samples, three metrics were extracted: the mean activation energy, μ_E, the standard deviation of activation energy, σ_E, and the activation energy at which CO_2 release reaches its peak, E_{max}.

2.4 Thermally sliced pyrolysis-gas chromatography-mass spectrometry (Ts-Py-GCMS)

Ts-Py-GCMS generates molecular fingerprints by thermally decomposing (in the absence of oxygen) non-volatile OM into volatile compounds, which are then separated by gas chromatography and identified via mass spectrometry based on molecular weight and fragmentation patterns (Derenne and Quéné, 2015; De Leeuw and Largeau, 1993; Lewis, 1993). Unlike more conventional flash pyrolysis methods, which generate a molecular fingerprint for one specific temperature (e.g., Kaal et al., 2009; Tolu et al., 2015), the Ts-Py-GCMS approach used here applies the same step-wise temperature windows as the ORO–AMS method. As for ORO-AMS, seven windows between 150 and 600 °C were analysed (150–240, 240–300, 300–350, 350–400, 400–455, 455–510, and 510–600 °C), together with an additional high-temperature window (600–850 °C) to capture the most thermally resistant components. No measurable carbon was detected below 150 °C. While the underlying processes differ (pyrolytic decomposition for Ts-Py-GCMS versus oxidative combustion for ORO–AMS and SoliTOC), the use of a common temperature framework provides a reference for comparison of trends across thermal windows, without implying direct equivalence of OM fractions.

Deleted: —

Deleted: —

Deleted: thermal windowseven without

Analyses were performed using an Agilent 7890A gas chromatograph (GC) coupled via a heated transfer line to a time-of-flight mass spectrometer (BenchTOF, Markes International). The GC was equipped with a Gerstel thermal desorption unit (TDU) pyrolysis system (Gerstel) connected to a cooled injection system (CIS), with a liquid nitrogen cryotrap for compound focusing (Gerstel). The pyrolysis unit operated in evolved gas analysis (EGA) mode with a heating rate of 1 °C s^{-1} and a maximum temperature of 850 °C. The CIS was initially cooled to −150 °C to trap the volatiles, followed by a fast-heating ramp to 320 °C with a 1-minute equilibration time, while the GC inlet temperature was maintained at 300 °C. Chromatographic separation was carried out using a DB5-ms column (30 m × 0.25 mm × 0.25 µm). The GC oven programme consisted of a 5-minute isothermal hold at 40 °C, followed by a ramp of 5 °C per minute to 270 °C, then 10 °C per minute to 320 °C with a final 10-minute hold. Each run lasted a total of 66 minutes.

Mass spectra were acquired using the BenchTOF instrument operating with an ionisation energy of 70 eV. The transfer line was maintained at 310 °C, and the ion source at 300 °C. The instrument scanned over an m/z range of 50 to 700 with a time-of-flight resolution better than 7,000 (full width at half maximum, FWHM) and mass accuracy within ±0.1 Da. Mass spectrometry data were processed using the OpenChrom software (Wenig and Odermatt, 2010), with compound identification aided by matching against the NIST23 Mass Spectral Library. Spectral matches were only considered valid when their match factor exceeded a reliability threshold of 70%, a commonly accepted cutoff for tentative identification (Bravo et al., 2017; Tolu et al., 2015). Compound identification and classification followed the approach described by Bravo et al. (2017) and Tolu et al. (2015), integrating match quality, literature-based retention-time patterns, and biomarker grouping to assign peaks to major OM compound classes. Because Ts-Py-GCMS involves thermal decomposition under oxygen-free conditions, charring and secondary pyrolysis reactions may occur, particularly at higher temperatures. Therefore, identified compounds are interpreted as operational pyrolysis products rather than direct molecular inventories of the original OM.

Compound classes identified in this study include branched/cyclic lipids (as markers of microbial origin or thermally altered OM) and *n*-alkyl lipids (straight-chain alkanes and alkenes derived from aliphatic biopolymers or thermally transformed OM). Lignin derivatives were used as biomarkers of vascular plant-derived OM (Kaal et al., 2016; Tolu et al., 2015). Pyrolysis products of carbohydrates and carbohydrate–cellulose derivatives (e.g., levoglucosan and furfural) were used to represent fresh biological inputs from plants or microbial exudates (Derenne and Quéné, 2015; Schnitzer and Monreal, 2011). Aromatic compounds, including phenols and polycyclic aromatic hydrocarbons (PAHs), derive from thermally stable precursor molecules that can form through microbial degradation, combustion, or advanced diagenesis and may also indicate mineral stabilisation of OM (Bravo et al., 2017; Kaal et al., 2009). Finally, N-containing compounds represent nitrogen-bearing molecules originating from microbial biomass, degraded proteinaceous material, or nitrogen-rich polymers such as chitin or peptidoglycans (Derenne and Quéné, 2015; Schnitzer and Monreal, 2011).

Deleted:

3 Results

3.1 OM thermal stability across thaw slump features

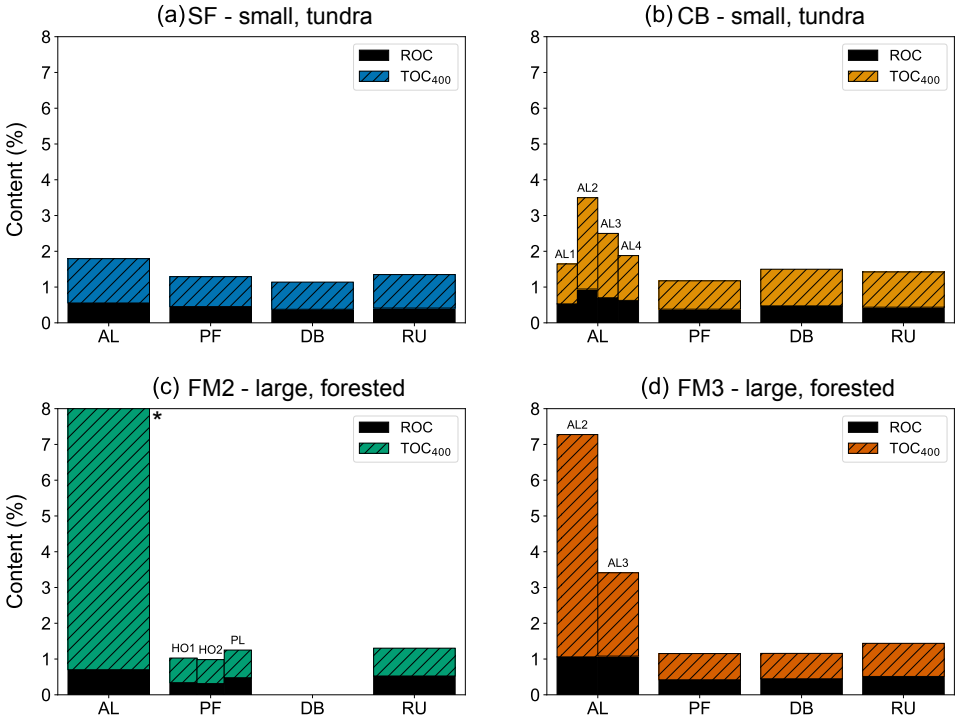

*Figure 2. Carbon content in thaw slump samples as measured by Solid total organic carbon (SoliTOC) analysis. Bars represent thermally labile organic carbon (TOC_{400}; coloured) stacked above residual organic carbon (ROC; black), expressed as percent (%) of C content. Each panel (a–d) corresponds to one thaw slump site—SF (blue), CB (yellow), FM2 (green), and FM3 (red)—with bars grouped by geomorphological feature: active layer (AL), permafrost (PF), debris (DB), and runoff (RU). For FM2, both Holocene and Pleistocene permafrost layers were accessible in the field and are shown separately. Where multiple samples were collected from the same feature, individual sample names are indicated above each bar. *The active layer sample from FM2 exhibited exceptionally high TOC_{400} content (>15%), far exceeding values measured in other geomorphological units or sites, and contributing to a combined TOC_{400} + ROC content of approximately 16%.*

Deleted: ¶

Across all four slumps, the DB, RU, and PF features exhibit relatively consistent TOC_{400} and ROC contents, with TOC_{400} generally between 1.1 and 1.3 %, and ROC between 0.5 and 0.8 % (Fig. 2). By contrast, the AL shows much greater variability across sites. In the smaller slumps (CB and SF), AL samples display TOC_{400} values around 1.5 % and ROC near 1.2 %, slightly higher than in the other features of those RTS. In the larger slumps (FM2 and FM3), however, AL TOC_{400} concentrations are markedly higher, ranging from 5 % to over 16 %, while ROC remains between 0.9 and 1.4 %.

The two largest slumps, FM2 and FM3, were selected for thermally sliced radiocarbon and chemical-fingerprint analysis because their well-developed geomorphic features (distinct AL, PF, DB, and RU zones) provide the most representative and internally consistent record of thaw-slump evolution across the Peel Plateau. Normalised CO_2 thermograms reveal distinct differences in thermal behaviour across geomorphic features and sites (Fig. 3a,c). Again, AL samples show the most pronounced contrasts. In both FM2 and FM3, CO_2 release begins early (between 170 and 200 °C) and peaks sharply at relatively low temperatures. The FM2 AL sample exhibits a dominant peak near 370 °C with a shoulder plateauing at ~400 °C, while FM3 AL2 and AL3 display bimodal structures: AL2 peaks at ~300 °C and ~450 °C, and AL3 at ~300 °C with a smaller secondary peak near 450 °C. These patterns correspond to comparatively low activation energies (FM2 AL: μ_E = 152 kJ mol^{-1}, E_{max} = 159 kJ mol^{-1}; FM3 AL2/AL3: μ_E = 152–156 kJ mol^{-1}, E_{max} = 140–173 kJ mol^{-1}). Activation-energy distributions are broader in AL samples ($\mu_E \approx$ 21–24 kJ mol^{-1}) than in PF-derived units, which show similarly elevated but more consolidated distributions ($\sigma_E \approx$ 17–24 kJ mol^{-1}).

In both slumps, PF samples (FM2 HO1, HO2, PL; FM3 HO) display broad, asymmetric peaks. CO_2 release begins gradually near 250 °C, peaks between 370 and 400 °C, and often shows a secondary shoulder near 470 °C with extended high-temperature tails. These features align with consistently higher activation energies than in AL samples ($\mu_E \approx$ 162–171 kJ mol^{-1}; $E_{max} \approx$ 155–161 kJ mol^{-1}). DB and RU samples follow similar trends to their corresponding PF layers. In FM3, both DB and RU thermograms closely resemble the HO profile and show similarly elevated activation-energy metrics ($\mu_E \approx$ 163–169 kJ mol^{-1}; $E_{max} \approx$ 155–161 kJ mol^{-1}). The FM3 RU sample exhibits an earlier onset of CO_2 release (~230 °C), with peaks between ~330 and 380 °C and a secondary shoulder near 450 °C. The FM2 RU sample departs slightly from this pattern, with a peak centred near 370 °C and a pronounced shoulder around 450 °C, accompanied by activation-energy values comparable to PF ($\mu_E \approx$ 167 kJ mol^{-1}; $E_{max} \approx$ 157 kJ mol^{-1}).

SoliTOC- and ORO–AMS–derived ROC/TOC ratios show consistent patterns across sample types, with higher values in PF, DB, and RU (ROC/TOC ≈ 0.25–0.45) and substantially lower values in AL (typically <0.15). However, ORO–AMS systematically yields higher absolute ROC/TOC values compared to SoliTOC (Fig. S2). Method-comparison analyses show that ROC/TOC patterns are robust across SoliTOC and ORO–AMS, whereas TIC-related metrics are method-dependent and therefore not used for interpretation; full details are provided in the Supplementary Material (Figs. S2–S4; Tables S2–S3).

Deleted: —

Deleted: —

Deleted: SoliTOC- and ORO–AMS–derived ROC/TOC ratios show consistent feature-level patterns, with higher values in PF, DB, and RU (ROC/TOC ≈ 0.25–0.45) and substantially lower values in AL (ROC/TOC typically <0.15), despite systematically lower absolute ROC/TOC values reported by ORO–AMS (Fig. S2).

3.2 Thermally-resolved radiocarbon signatures

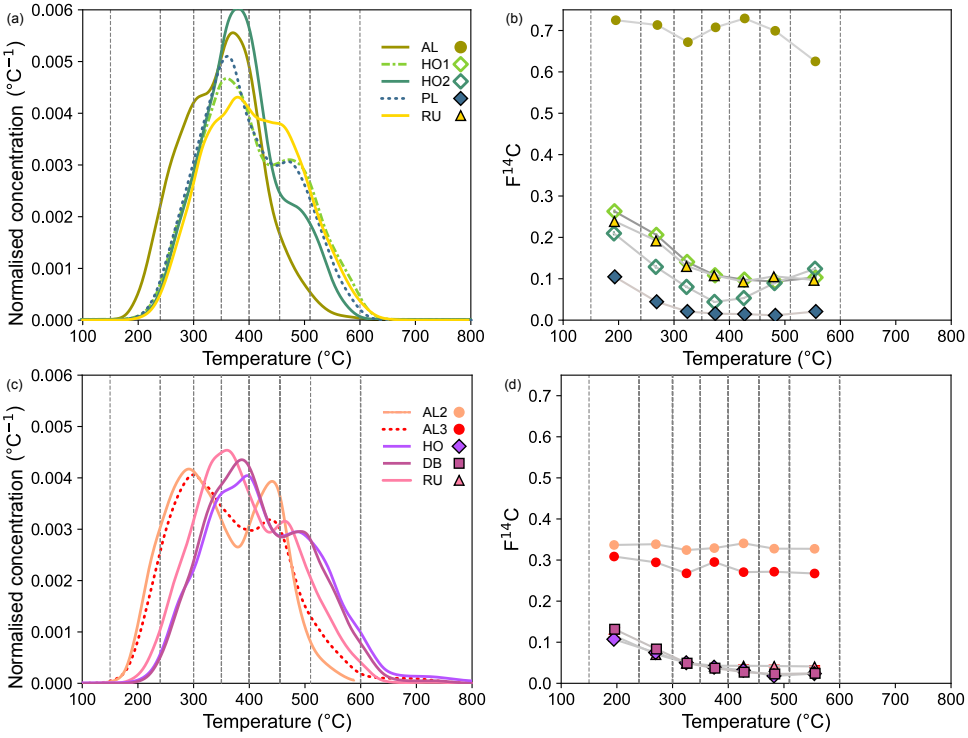

Figure 3. Panels (a) and (c): Thermograms showing the concentration of CO_2 (as area normalized concentration per °C) as a function of temperature during progressive thermal oxidation of samples from thaw slumps FM2 (a) and FM3 (c). Colours indicate feature type: active layer (AL), debris (DB), runoff (RU), and permafrost (PF), including Holocene (HO) and Pleistocene (PL) samples and line styles distinguish samples with the same geomorphological feature. All thermograms are normalised to the same integrated area, following the method of Hemingway et al. (2017). (b) and (d) Radiocarbon content ($F^{14}C$) measured across thermal decomposition windows for FM2 (b) and FM3 (d). Symbol shapes represent geomorphological features: circle = AL, square = DB, triangle = RU, diamond = PF (for FM2 - open = HO; filled = PL) and measurement uncertainties are too small to be displayed.

Deleted: concetration

Deleted: .

Radiocarbon age distributions across the thermal lability spectrum were analysed for a subset of samples from the two largest slumps, FM2 and FM3 (Fig. 3b,d; Figs. S5-S14; Table S3). The FM2 AL exhibits a modest decline in $F^{14}C$ values with increasing temperature from 0.725 ± 0.008 at 150–240 °C to 0.625 ± 0.007 at 510–600 °C. (Fig. 3b). A minor decrease also occurs at 300–350 °C (0.672 ± 0.008), followed by the highest $F^{14}C$ at 400–455 °C (0.729 ± 0.008) and a gradual decline at higher temperatures. By contrast, AL samples from FM3 (Fig. 3d) show consistently lower $F^{14}C$ values. FM3 AL2 remains relatively stable, ranging from 0.337 ± 0.005 at 150–240 °C to 0.327 ± 0.006 at 510–600 °C, while AL3 is even more ^{14}C-depleted, ranging from 0.309 ± 0.006 to 0.267 ± 0.007, with no significant trend over the thermal range.

Across PF, DB, and RU, $F^{14}C$ generally decreases with increasing temperature (Fig. 3b,d). The trend is clearest in PF samples; e.g., in FM2 (Fig. 3b), HO1 $F^{14}C$ values decrease from 0.262 ± 0.005 to 0.102 ± 0.004, HO2 from 0.209 ± 0.005 to 0.123 ± 0.004, and the PL layer reaches 0.015–0.021 in the highest temperature windows, indicating near-radiocarbon-free material. Interestingly, the FM2 HO2 profile shows a partial reversal, with $F^{14}C$ reaching a minimum at 350–400 °C (0.042 ± 0.002) before rising to 0.123 ± 0.004 at 510–600 °C. FM3 HO (Fig. 3d) exhibits a similar depletion trend, decreasing from 0.106 ± 0.004 to 0.023 ± 0.002, with a signal near radiocarbon-dead for the highest temperature window.

In FM2, the RU sample exhibits a pronounced decline in $F^{14}C$ from 0.239 ± 0.006 to 0.097 ± 0.003 across the thermal windows, a pattern closely resembling the behaviour of the HO1 layer rather than the deeper PL PF. In FM3, both DB and RU decrease from initial values of ~0.13 and ~0.12 to 0.025 and 0.041, respectively, at 510–600 °C, which is almost identical to HO PF. Together, these patterns show that $F^{14}C$ generally decreases with increasing thermal resistance across most features, with the exception of the AL and a partial rebound observed in the HO2 profile. Finally, weighted-average bulk $F^{14}C$ reconstructed from all ORO–AMS thermal windows closely match independent EA–AMS bulk measurements (Fig. S1; R^2 = 0.99, RMSD ≈ 0.03), demonstrating that the thermal-integration approach reproduces bulk $F^{14}C$ within analytical uncertainty.

Deleted: Together, these patterns show that $F^{14}C$ systematically decreases with thermal resistance across all features except the AL.

3.3 OM molecular fingerprinting across thermal windows

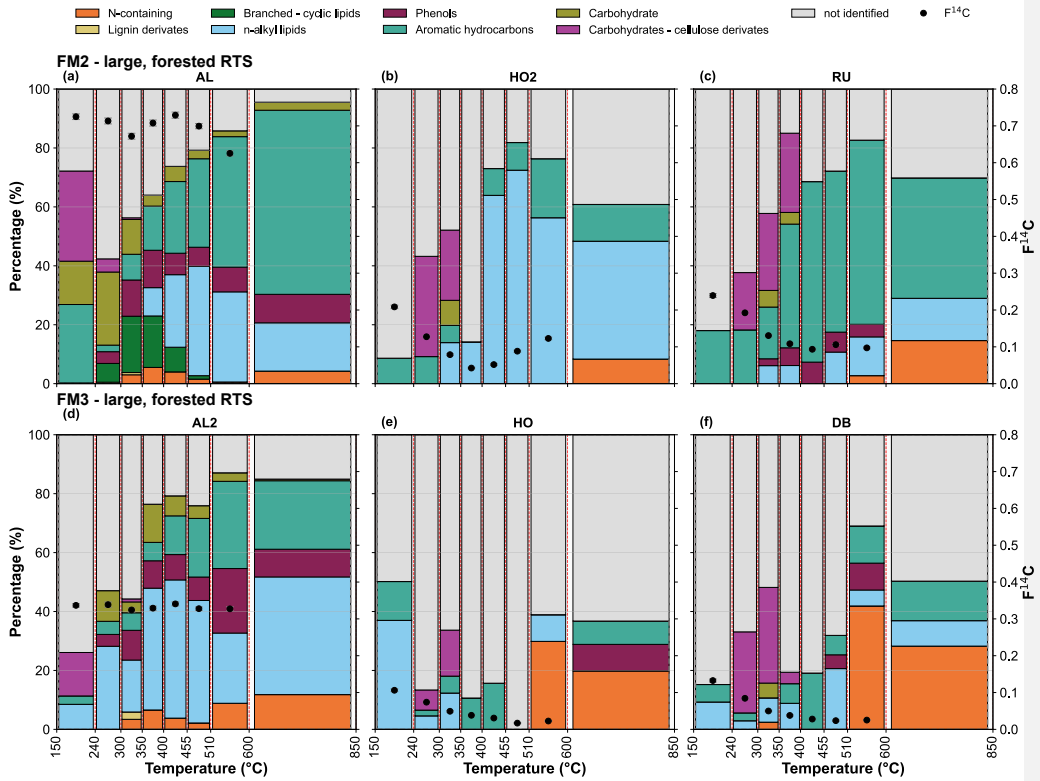

Figure 4. Normalized peak area distributions of molecular compound classes across thermal windows (150–850 °C) for selected thaw slump features (a - c) FM2: active layer (AL), deeper Holocene permafrost (HO2), and runoff (RU). (d - f) FM3: active layer (AL2), Holocene permafrost (HO), and debris (DB). Compound classes include nitrogen-containing compounds, lignin derivatives, branched–cyclic lipids, n-alkyl lipids, phenols, aromatic hydrocarbons, carbohydrates, and cellulose derivatives, with the $F^{14}C$ fractions measured with ORO on the right. The combined presentation is intended to relate molecular composition to thermal stability and radiocarbon age, rather than to imply direct equivalence between fractions obtained by pyrolysis and combustion-based methods.

Formatted: Font: Italic

Formatted: Justified, Line spacing: 1.5 lines

Formatted: Font: Italic

Formatted: Font: Times New Roman, 10 pt, Italic, Font color: Auto

Deleted: ¶

Interpretable Ts-Py-GCMS chromatograms were obtained for (almost) all thermal windows of AL, HO2 and RU from FM2 and AL2, AL3, HO and DB from FM3 (Fig. 4), whereas other samples (FM2 HO1 and PL, FM3 RU) did not yield usable data due to low signal intensity or excessive noise in most thermal windows (Figs. S15–S16). Compound-class distributions generally reflected a progressive shift from labile, oxygen-rich OM at low temperatures to more compositionally altered, thermally stable material at higher temperatures across all thaw-slump components (peak lists for all analysed samples are provided in Table S4). To facilitate interpretation across methods, molecular compound-class distributions are presented alongside $F^{14}C$ values derived from ORO–AMS for corresponding temperature intervals, providing a combined view of OM composition, thermal stability, and radiocarbon age.

In FM2 (Fig. 4a–c), AL, HO2, and RU samples display temperature-dependent shifts in the proportions of specific compound classes. Groups indicating fresh (and potentially bioavailable) OM such as carbohydrates, including cellulose-derived compounds, dominate the 240–300 °C window but are largely absent above 510 °C. Phenols occur across the full thermal range, with variable intensities among geomorphic features, whereas lignin derivatives are detected only in the AL sample. In contrast, proportions of *n*-alkyl lipids and aromatic hydrocarbons increase progressively with temperature, becoming most abundant between 510 and 600 °C. N-containing compounds appear mainly at mid to high temperatures (300–510 °C) and re-emerge in AL and RU in the highest temperature window (600-850 °C). More specifically, the AL sample contains abundant hemicellulose- and cellulose-derived carbohydrates within the 240–300 °C window (e.g., xylose, arabinose, glucose, furfural), followed by phenols 300-350 °C and a distinct shift toward aliphatic lipids and aromatic hydrocarbons between 400 and 510 °C. HO2 contains furfural and branched–cyclic lipids 300-350 °C, transitioning to *n*-alkyl lipids and aromatics in the 510–850 °C range. RU displays methylstyrene compounds at 240–300 °C, cellulose pyrolysis products between 300–350 °C, and increasingly aromatic profiles above 455 °C, with mainly condensed PAHs at 850 °C.

In FM3 (Fig. 4d–f), AL2 (Fig. 4d) and AL3 (Fig. S16) exhibited compound-class distributions broadly consistent with those observed for FM2 AL, with a clear progression from carbohydrates and phenols at lower temperatures to increasing contributions of aliphatic lipids and aromatic compounds at later thermal intervals. Between 350–400 °C, both AL2 and AL3 transitioned toward more thermally stable compounds, with rising proportions of phenols, *n*-alkyl lipids, and aromatics. Above 455 °C, PAHs and N-containing compounds became dominant, particularly in AL3. In contrast, the HO and DB samples (Fig. 4e–f) exhibited an earlier release of hydrocarbons and *n*-alkyl lipids already within the 150–240 °C window. Carbohydrates were largely absent from HO but appeared in DB above 350 °C, while phenols and N-containing compounds were mainly detected at higher temperatures. Chromatograms from the 455–510 °C interval in HO did not yield reliable compound matches. At lower temperatures (240–300 °C), cellulose pyrolysis products (e.g., furfural), methylstyrene compounds, and short- to mid-chain *n*-alkyl lipids occurred across AL2, AL3, HO, and DB. AL2 and AL3 also contained phenols consistent with lignocellulose decomposition. Both HO and DB yielded *n*-aldehydes and levoglucosan, while DB additionally released nonanal and decanal already at 240–300 °C. At the highest temperatures (600–850 °C), persistent compounds included long-chain *n*-alkyl lipids, condensed aromatics (e.g., naphthalene derivatives), and N-containing compounds, representing the residual products of OM decomposition.

Deleted: organic matter
Deleted: OM
Deleted:
Deleted:
Deleted:

4 Discussion

4.1 OM stability mechanisms across geomorphic features

Thermal behaviour, radiocarbon patterns, and molecular compositions together show that fundamentally different OM pools are present within the different geomorphic features of the four slumps (Figs. 2–4). Thermograms from FM2 and FM3 demonstrate that AL material begins oxidising at much lower temperatures than PF, DB and RU and exhibits a distinct structure, expressed either as a sharp early peak or as a bimodal profile with comparable low- and mid-temperature contributions (Fig. 3a,c). These patterns are consistent with lower mean activation energies in AL samples ($\mu_E \approx 152–156$ kJ mol^{-1}) and, particularly in FM3, broader activation-energy distributions ($\sigma_E \approx 21–24$ kJ mol^{-1}), reflecting energetically heterogeneous and comparatively reactive OM pools. In contrast, PF, DB, and RU samples show later onsets of CO_2 release, unimodal peaks centred near ~370–400 °C and pronounced high-temperature tails characteristic of thermally stable carbon. These features coincide with higher μ_E values (≈ 162–171 kJ mol^{-1}) and consistently elevated but more uniform σ_E values (≈ 17–24 kJ mol^{-1}) across deeper units, indicating a dominance of energetically resistant OM with less variability in stabilisation mechanisms than observed in the AL.

Py-GCMS molecular fingerprints provide a compositional context for these contrasting thermogram shapes when evaluated within the common temperature framework (Fig. 4). In low-temperature windows (240–350 °C), AL samples are relatively enriched in carbohydrate- and cellulose-derived pyrolysates compared to PF, DB, and RU, consistent with the dominance of recently produced, oxygen-rich OM that oxidises early. At higher temperatures (>455 °C), all features show increasing contributions from aromatic hydrocarbons and long-chain n-alkyl lipids; however, these compounds dominate the high-temperature fractions of PF, DB, and RU, whereas AL retains a more mixed molecular signature. This enrichment of condensed and lipid-rich structures in PF-derived material aligns with their broad thermogram peaks and extended high-temperature tails. Similar temperature-dependent compositional shifts have been reported for permafrost OM elsewhere, where aromatic and lipid-rich components control high-temperature reactivity (Tolu et al., 2015; Zaccone et al., 2011). Together, these observations identify the primary molecular divide between biologically active surface horizons and deeper, cryogenically preserved permafrost-derived pools.

Radiocarbon profiles across thermal windows reinforce this interpretation (Fig. 3b,d). AL samples in FM2 maintain high $F^{14}C$ values (~0.73–0.63), whereas the FM3 AL samples show lower values (~0.33–0.27), reflecting that AL2 and AL3 were collected from deeper positions within the active layer than the surface AL sampled at FM2, leading to smaller contributions of recent vegetation and instead greater contributions of older, legacy OM. Although AL samples from both RTS do not display strictly invariant $F^{14}C$ values across thermal windows, they show only modest variation relative to PF, DB and RU samples, and several AL fractions as well as the FM2 HO2 sample even show local increases in $F^{14}C$ with increasing temperature, indicating that a small fraction of comparatively young OM persists into higher-temperature (higher-energy)

Deleted: lopwer

Deleted: ,

Deleted: Py-GCMS molecular fingerprints provide a mechanistic explanation for these contrasting thermogram shapes when compared within equivalent thermal windows

Deleted: .

Deleted: .

windows. Such complexity suggests that much of the carbon oxidised across low- to mid-temperature windows derives from surface-influenced or recently cycled sources with overlapping activation-energy domains rather than a simple "young = low-T / old = high-T" structure. Also, $F^{14}C$ values are very different between AL samples from FM2 and FM3; this aligns with cryoturbated or compositionally heterogeneous soil horizons within this seasonally thawed layer, where young and older OM can co-occur within similar energetic ranges. In contrast to AL samples, PF, DB and RU display systematic and often steep declines in $F^{14}C$ with increasing temperature, consistent with sequential oxidation of progressively older and more refractory pools.

Activation energy-resolved $F^{14}C$ spectra further support these trends (Figs. S17–S18). AL material retains high to intermediate $F^{14}C$ across low-to-mid E, with only a minor old fraction emerging in the high-E tail. In contrast, PF, DB and RU are uniformly depleted across nearly the entire $p(0,E)$ spectrum, with the strongest depletion at highest E values, indicating that the most oxidation-resistant fractions are also the oldest. FM3 AL horizons show large σ_E values (≈ 21–24 kJ mol^{-1}), reflecting substantial internal heterogeneity due to mixed plant inputs, cryoturbation, and variable degrees of protection. These energetic patterns highlight that OM stability arises from interactions between molecular composition, cryogenic preservation, and physical or mineral protection (Grant et al., 2019; Hemingway et al., 2017, 2019).

Similarly, μ_E vs. bulk $F^{14}C$ relationships reveal clear clustering (Supplementary materials Figs. S17-18). AL samples from both slumps occupy a low μ_E, high $F^{14}C$ domain, whereas PF, DB and RU plot consistently at higher μ_E and lower $F^{14}C$. As expected, these patterns mirror the thermogram shapes and activation-energy spectra: low μ_E values reflect lower kinetic barriers associated with labile or less-protected material, whereas high μ_E values reflect the stronger stabilisation of permafrost-derived pools. σ_E patterns follow the same structure: broader distributions in AL, narrower ones in PF-derived material. Exceptions—including the HO_2 high-E young fraction and several AL windows containing young OM at higher temperatures—likely reflect the presence of protected or mineral-associated OM within active-layer and upper-permafrost horizons.

Across both slumps, $F^{14}C$ decreases systematically with increasing μ_E (Fig. 5a). The corresponding μ_E –ROC/TOC relationship (Fig. S19) shows that these energetic differences are reflected in operational thermal recalcitrance: AL consistently exhibits low ROC/TOC values at low μ_E, whereas PF and mobilised units DB and RU occupy a high-ROC/TOC, high-μ_E field. Importantly, these relationships describe feature-level end-member behaviour rather than within-feature structure. As shown above, individual AL samples can host young and old carbon across overlapping activation-energy ranges and thus do not follow a strict "young = low-T / old = high-T" rule. Instead, these broader μ_E–$F^{14}C$ and μ_E–ROC/TOC trends emerge when contrasting surface versus permafrost-derived pools at the scale of geomorphic units. Together, these trends define two internally coherent stability domains—"young and labile" versus "old and recalcitrant"—within which OM from FM2 and FM3 can be consistently interpreted. Having established these domains for the two fully characterised slumps, we now extend the comparison to all four RTS using the bulk metrics (ROC/TOC and bulk $F^{14}C$) available across sites.

Deleted: reinforce

Deleted: in energy space

Deleted: .

Deleted:

Deleted: AL samples consistently occupy a low- μ_E, high-$F^{14}C$ domain, whereas PF, DB and RU plot toward higher μ_E and lower $F^{14}C$. …

Formatted: Subscript

Deleted: likely

Deleted: carbon

Deleted: OM

Deleted: ,

Deleted: internally

Deleted: the

Formatted: Font: Italic, Subscript

Formatted: Font: Italic, Subscript

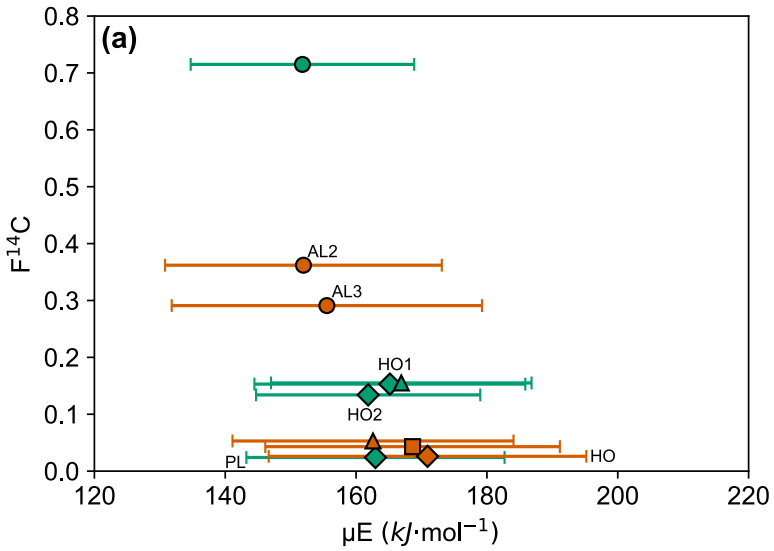
(a)
0.8
0.7
0.6
0.5
0.4
0.3
0.2
0.1
0.0
F14C
AL2
AL3
HO1
HO2
PL
HO
120
140
160
180
200
220
μE (kJ·mol−1)

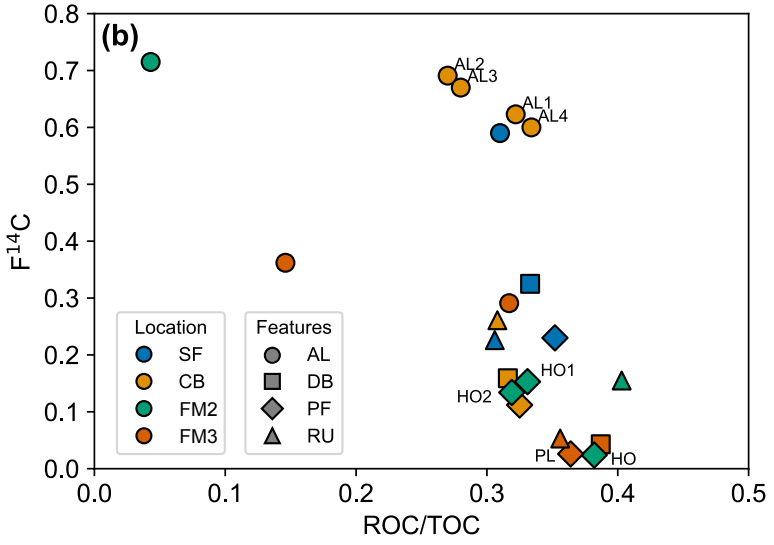
(b)
0.8
0.7
0.6
0.5
0.4
0.3
0.2
0.1
0.0
F14C
AL2
AL3
AL1
AL4
HO1
HO2
PL
HO
Location
SF
CB
FM2
FM3
Features
AL
DB
PF
RU
0.0
0.1
0.2
0.3
0.4
0.5
ROC/TOC

Figure 5. Panel (a) Relationship between $F^{14}C$ and mean activation energy (μ_E) across thaw slump samples from the Peel Plateau. Horizontal error bars represent the standard deviation (σ_E) of the activation energy distributions, reflecting the energetic heterogeneity of OM thermal decomposition. Panel (b) Bulk $F^{14}C$ values (from Bröder et al., 2021) are compared with ROC/TOC ratios from SoliTOC measurements (see definition in the text) across four thaw slump locations and their respective features. Different features are indicated by shapes: circles represent active layer (AL), squares debris (DB), diamonds permafrost (PF), and triangles runoff (RU). Colours correspond to sampling locations: blue for SF, orange for CB, green for FM2, and red for FM3.

Deleted: *organic matter*

4.2 RTS-scale differences in thermal lability and radiocarbon

Across the Peel Plateau sites, ROC/TOC ratios (from SoliTOC analyses) and bulk $F^{14}C$ patterns reveal that slump morphology, vegetation, and active-layer thickness regulate only the surface OM pools, whereas deeper permafrost-derived material remains compositionally and thermally uniform (Fig. 5b). At the forested slumps FM2 and FM3, AL horizons show higher TOC_{400} and distinct radiocarbon signatures that reflect greater biological inputs and deeper seasonal thaw. FM2 AL is the youngest and most labile, consistent with substantial modern vegetation input. FM3 AL is more heterogeneous because AL2/AL3 samples were collected at greater depths within this cryoturbated layer containing a mix of young and older OM. In contrast, CB and SF—both tundra sites with thin active layers—show lower TOC_{400} but still young bulk $F^{14}C$, indicating low OM input rather than rapid turnover. Despite this ecological variability at the surface, PF, DB, and RU units from all four RTS consistently exhibit higher ROC/TOC and lower bulk $F^{14}C$, showing that the deep, cryogenically preserved, low-OC permafrost substrate mobilised by abrupt thaw and erosion is effectively invariant across the region.

Deleted: .

These across-slump differences are most clearly expressed when bulk age and thermal partitioning are combined in ROC/TOC–$F^{14}C$ space (Fig. 5b). AL samples from all RTS plot within a "young, thermally labile" domain, but their position reflects ecological setting: FM2 AL is the youngest and most labile; FM3 AL is moderately depleted and intermediate in stability; and tundra AL (CB/SF) is more thermally resistant yet still young in radiocarbon age owing to limited biological input. In contrast, PF, DB and RU from every slump occupy a compact, old and recalcitrant cluster. This demonstrates that the mechanistic distinctions identified previously are not site-specific: the PF–DB–RU continuum forms a consistent, regionally coherent stability field regardless of vegetation, or slump size. This pattern aligns with prior studies showing that RTS in the Peel Plateau predominantly mobilise radiocarbon-depleted particulate OM from deeper permafrost with limited compositional alteration during initial transport (Bröder et al., 2021; Keskitalo et al., 2021; Shakil et al., 2020; Zolkos et al., 2019).

Overall, RTS-scale contrasts indicate that ecological setting and slump morphology primarily influence the composition and stability of active-layer OM, whereas deeper permafrost-derived pools exhibit consistent thermal and radiocarbon behaviour across all slumps. Importantly, all four RTS display uniformly low TOC in PF (HO and PL), DB and RU units, with no evidence for peat-rich or historically high-productivity ecosystems. This pattern aligns with regional mapping and previous

work showing that the Peel Plateau is largely underlain by glacial/moraine-derived, ice-rich sediments rather than organic-rich deposits (Kokelj et al., 2017; Zolkos et al., 2018). The uniformity of PF-derived material across slumps therefore reflects mobilisation of a broadly homogeneous, low-OC, cryogenically preserved substrate, setting the stage for evaluating its regional carbon-cycle significance in the next section.

4.3 RTS carbon in regional and circumpolar context

Distilling the feature-level and RTS-level patterns into a regional perspective shows that slumps on the Peel Plateau primarily mobilise old, thermally stable permafrost-derived carbon, reflecting both their geomorphic configuration and the moraine–till substrate underlying soils of the region. Across FM2, FM3, CB and SF, deeper PF—as well as mobilised components DB and RU—consistently share low bulk $F^{14}C$, high ROC/TOC and high $\mu\varepsilon$ (Fig. 5; Figs. S17–S19), indicating mobilisation and export of a broadly uniform pool of previously cryogenically preserved, relatively oxidation-resistant OM. These signatures match regional observations that Peel Plateau slumps export particulate OM largely originating from permafrost layers exposed at the headwalls rather than recently produced vegetation or active-layer material (Bröder et al., 2021; Keskitalo et al., 2021; Shakil et al., 2020; Zolkos et al., 2019).

The RU samples therefore represent an important transitional pool linking mobilisation of terrestrial material to riverine export and potential in-stream processing. Their similarity to PF and DB material indicates that runoff exports old, thermally stable particulate OM with limited alteration during early mobilisation. This material may be transported downstream and deposited in riverine, deltaic, or coastal sediments, acting as a transient or longer-term particulate carbon sink. However, river systems are not passive conduits: hydrodynamic sorting, oxygen exposure, changes in mineral association, and microbial processing may alter OM reactivity during transport. Under such variable conditions, parts of this thermally stable, aged carbon could still be transformed into dissolved or gaseous forms and contribute to a translocated, delayed greenhouse-gas release, as recently suggested for aged carbon leakage from the Mackenzie River system (Dasari et al., 2024).

The stability of the exported OM is further supported by incubation studies from the Peel Plateau and comparable moraine–till permafrost settings elsewhere in the Arctic. Laboratory and field incubations on mineral-rich permafrost soils from north-west Canada, Alaska, and other glaciated terrains demonstrate that respiration-resistant carbon pools are dominated by mineral-associated and physically protected fractions, while only a small labile component is rapidly decomposed following thaw (Estop-Aragonés et al., 2020; Littlefair et al., 2017; Schädel et al., 2014; Vaughn and Torn, 2019). These systems are characterised by relatively low TOC and strong mineral control on OM stabilisation, closely matching the geomorphic and substrate conditions of the Peel Plateau. The persistence of old, high- $\mu\varepsilon$, high-ROC/TOC carbon in PF, DB and RU observed here mirrors these results, indicating that slump processes in this region primarily redistribute protected permafrost material downslope with minimal compositional alteration, rather than triggering substantial early-stage degradation. These findings contrast with observations made for so-called Yedoma permafrost. This late Pleistocene, syngenetic, silt-dominated, ice-rich

Deleted: ,
Deleted: RU
Deleted: ,
Deleted: Importantly, the uniformly low TOC contents in PF, HO, DB and RU across all slumps further show that neither FM2/FM3 nor CB/SF host significant extents of peat-rich or historically productive ecosystems—consistent with a glacial–moraine, ice-rich substrate.
Formatted: Font: Not Italic
Deleted: organic
Deleted: -
Deleted: carbon concentrations

permafrost contains some of the highest TOC and ground-ice contents in the Arctic, storing ~327–466 Gt C globally and representing up to one-third of the deep-frozen carbon pool (Martens et al., 2023; Strauss et al., 2017, 2025). This substrate contrast has direct implications for carbon dynamics: erosion of Yedoma deposits can mobilise extremely carbon-rich and comparatively microbially labile OM, as shown by incubation and field studies reporting high respiration rates and rapid carbon losses following thaw (Knoblauch et al., 2013; Strauss et al., 2017; Vonk et al., 2013). In contrast, thaw slumps developed in moraine–till terrains mobilise permafrost carbon characterised by lower TOC concentrations and strong mineral association, resulting in compositionally uniform, physically protected OM that resists rapid oxidation. Substrate type therefore plays a central role in determining the fate of eroded permafrost OM and must be explicitly considered when extrapolating thaw-slump impacts to the pan-Arctic scale.

5 Conclusions

Across thermal, isotopic, and molecular measurements, our results show that organic-matter stability in Peel Plateau thaw slumps is primarily structured by geomorphic origin and protection state, with a clear contrast between active-layer material and permafrost-derived carbon. The active layer contains younger and more reactive OM influenced by contemporary vegetation inputs, but cryoturbation and increasing sampling depth allow older, legacy carbon to contribute within this horizon. In contrast, permafrost material is uniformly radiocarbon-depleted, thermally stable, and compositionally resistant. The similarity to debris and runoff indicates largely downslope mobilisation of permafrost-derived OM rather than in situ decomposition.

Thermal resistance and $F^{14}C$ activity generally covary across these features, but not through a simple ordering of "young = low *E*" and "old = high *E*." Activation energy-resolved $F^{14}C$ spectra and Ts-Py-GCMS compound classes show that young and old fractions can overlap in energetic space due to mineral association, aggregation, and cryogenic preservation. This explains why AL horizons can retain stabilised, higher-energy fractions, and why PF horizons include components of differing energetic stability. Despite this heterogeneity, PF, DB, and RU consistently occupy high-energy, radiocarbon-depleted domains, while AL remains restricted to lower-energy, younger or intermediate-age spaces, confirming that the dominant controls on OM stability lie in source, composition, and degree of protection.

A key outcome is that early-stage RTS mobilisation does not substantially alter the thermal stability or radiocarbon characteristics of PF-derived particulate OM. Instead, slumping primarily redistributes compositionally resistant, ancient carbon downslope with little evidence for rapid transformation, consistent with observations from other mass-wasting–dominated systems with similar geological settings. These patterns are consistent across all four RTS (FM2, FM3, CB, and SF), despite pronounced ecological differences in active-layer composition. Forested and tundra slumps show contrasting AL properties, but their PF horizons, as well as thaw-eroded debris (DB) and exported runoff material (RU), are characterised by uniformly old, thermally stable, and low-TOC substrates. This convergence across sites reflects the shared glacial–moraine,

Deleted: and

Deleted: Mapping studies show that the vast majority of Yedoma occurs in North Asia, whereas the Canadian share is small and spatially restricted

Deleted: .

Deleted: organic matter

Deleted: lowerlow

Deleted: —and the debris and runoff derived from it—

Deleted: ,

Deleted: ing, indicating

Deleted: that debris and runoff

Deleted: reflect

Deleted: distinct carbon pools

Deleted: .

Deleted: In this study, resistance to degradation is inferred from thermal and isotopic proxies rather than direct measurements of mineralisation

Deleted: ,

Deleted: and thus reflects OM persistence rather than instantaneous CO_2 production.

Deleted: —

Deleted: —)—

ice-rich geological setting of the Peel Plateau. Unlike Yedoma, which consists of thick, syngenetic, ice-rich, and carbon-dense deposits, moraine/till terrains host lower-TOC, cryogenically reworked material with distinct stabilisation histories. RTS developed in such substrates therefore likely mobilise a fundamentally different permafrost carbon pool than Yedoma-derived slumps. Predicting the fate of thaw-mobilised permafrost carbon thus requires integrating OM age, composition, and energetic stability within geomorphic context. By resolving how these properties co-vary across RTS features and across slump types, this study provides a mechanistic basis for understanding why RTS preferentially export long-preserved, protected OM and how these processes shape downstream carbon fluxes in glacial-moraine landscapes. Such structure-informed perspectives are essential for constraining Arctic carbon-cycle feedbacks under continued warming.

Deleted: , with important implications for how thaw-mobilised carbon is redistributed and for how RTS impacts should—and should not—be generalised across the Arctic

Deleted: ¶

5.1.1 Data availability

Additional data are provided in the supplementary material.

5.1.2 Author contributions

LB secured project funding. LB, KK and JV supplied materials and contributed to the description of sample context. MB conducted the majority of measurements, with guidance from NH for the radiocarbon analyses, and performed sample preparation together with NH. TE assisted with Ts-Py-GCMS data interpretation, and JDH provided expertise on the energy distribution analysis. MB led the manuscript writing, with all authors contributing to data interpretation and providing critical feedback on the analysis and manuscript.

5.1.3 Competing interests

The authors declare that they have no conflict of interest.

5.1.4 Acknowledgements:

We thank Thomas Blattmann for laboratory and technical support with the Ts-Py-GCMS analyses; Irene Brunner and Nathalie Dubois for conducting the SoliTOC measurements at EAWAG; and Philip Wenig for providing guidance on OpenChrom use. We are grateful to Sebastian Näher for insightful discussions and suggestions on how to interpret the GC/MS data, and to Urs Ramsperger, Lukas Wacker, and the LIP staff for their assistance with AMS measurements. Special thanks go to Daniele De Maria for his early support in setting up and troubleshooting the DTI interface.

5.1.5 Financial support

This research was funded by the Swiss National Science Foundation (SNF – grant no. 200021-204093 awarded to L.B.). Additional support was provided by the facilities and infrastructure of ETH Zurich, which enabled the analytical and laboratory

work presented in this study. J.D.H. acknowledges funding from the European Research Council (ERC) under the European Union's Horizon 2020 research and innovation program (Grant agreement No 946150). J. E. Vonk acknowledges funding from a European Research Council (ERC) Starting Grant (THAWSOME, grant no. 676982). K. Keskitalo further acknowledges funding from the Nederlandse Organisatie voor Wetenschappelijk Onderzoek (NWO, Dutch Research Council; Rubicon grant no. 019.212EN.033).

5.1.6 Review statement:

This paper was edited by Darci Rush and reviewed by two anonymous referees. The evaluation process was carried out in the open discussion forum of Biogeosciences.

Deleted: J.D.H. acknowledges funding from the European Research Council (ERC) under the European Union's Horizon 2020 research and innovation program (Grant agreement No 946150). K. Keskitalo and

Deleted: J. E. Vonk

Deleted: [Editor's Name]

Deleted: [number]

Deleted: 2

References

Abbott, B. W., Larouche, J. R., Jones, J. B., Bowden, W. B., and Balser, A. W.: Elevated dissolved organic carbon biodegradability from thawing and collapsing permafrost, J. Geophys. Res. Biogeosci., 119, 2049–2063, https://doi.org/10.1002/2014JG002678, 2014.

Bockheim, J. G. and Tarnocai, C.: Recognition of cryoturbation for classifying permafrost-affected soils, Geoderma, 81, 281–293, https://doi.org/10.1016/S0016-7061(97)00115-8, 1998.

Bolandini, M. A., De Maria, D., Haghipour, N., Wacker, L., Hemingway, J. D., Eglinton, T. I., and Bröder, L.: Towards online ramped oxidation (ORO)-AMS for thermal dissection and serial radiocarbon analysis of complex organic matter, Radiocarbon, 1–16, https://doi.org/10.1017/RDC.2025.6, 2025.

Bravo, A. G., Bouchet, S., Tolu, J., Björn, E., Mateos-Rivera, A., and Bertilsson, S.: Molecular composition of organic matter controls methylmercury formation in boreal lakes, Nat. Commun., 8, 1–9, https://doi.org/10.1038/NCOMMS14255, 2017.

Bröder, L., Keskitalo, K. H., Zolkos, S., Shakil, S., Tank, S. E., Kokelj, S. V., Tesi, T., Van Dongen, B. E., Haghipour, N., Eglinton, T. I., and Vonk, J. E.: Preferential export of permafrost-derived organic matter as retrogressive thaw slumping intensifies, Environmental Research Letters, 16, 054059, https://doi.org/10.1088/1748-9326/ABEE4B, 2021.

Dasari, S. and Widory, D.: Radiocarbon (14C) Analysis of Carbonaceous Aerosols: Revisiting the Existing Analytical Techniques for Isolation of Black Carbon, Front. Environ. Sci., 10, 907467, https://doi.org/10.3389/FENVS.2022.907467, 2022.

Dasari, S., Garnett, M. H., and Hilton, R. G.: Leakage of old carbon dioxide from a major river system in the Canadian Arctic, PNAS Nexus, 3, https://doi.org/10.1093/PNASNEXUS/PGAE134, 2024.

Derenne, S. and Quéné, K.: Analytical pyrolysis as a tool to probe soil organic matter, J. Anal. Appl. Pyrolysis, 111, 108–120, https://doi.org/10.1016/J.JAAP.2014.12.001, 2015.

Drake, T. W., Wickland, K. P., Spencer, R. G. M., McKnight, D. M., and Striegl, R. G.: Ancient low-molecular-weight organic acids in permafrost fuel rapid carbon dioxide production upon thaw, Proceedings of the National Academy of Sciences, 112, 13946–13951, https://doi.org/10.1073/PNAS.1511705112, 2015.

Estop-Aragonés, C., Olefeldt, D., Abbott, B. W., Chanton, J. P., Czimczik, C. I., Dean, J. F., Egan, J. E., Gandois, L., Garnett, M. H., Hartley, I. P., Hoyt, A., Lupascu, M., Natali, S. M., O'Donnell, J. A., Raymond, P. A., Tanentzap, A. J., Tank, S. E., Schuur, E. A. G., Turetsky, M. R., and Anthony, K. W.: Assessing the Potential for Mobilization of Old Soil Carbon After Permafrost Thaw: A Synthesis of 14C Measurements From the Northern Permafrost Region, Global Biogeochem. Cycles, 34, e2020GB006672, https://doi.org/10.1029/2020GB006672, 2020.

French, H. M.: The periglacial environment, Wiley, Chichester, UK, 459, 2007.

Garnett, M. H., Pereira, R., Taylor, C., Murray, C., and Ascough, P. L.: A new ramped oxidation -14C analysis facility at the NEIF Radiocarbon Laboratory, East Kilbride, UK, Radiocarbon, 65, 1213–1229, https://doi.org/10.1017/RDC.2023.96, 2023.

Grant, K. E., Galy, V., Chadwick, O. A., and Derry, L. A.: Thermal oxidation of carbon in organic matter rich volcanic soils: insights into SOC age differentiation and mineral stabilization, Biogeochemistry, 144, 291–304, https://doi.org/10.1007/S10533-019-00586-1, 2019.

Harris, D., Horwáth, W. R., and van Kessel, C.: Acid fumigation of soils to remove carbonates prior to total organic carbon or CARBON-13 isotopic analysis, Soil Science Society of America Journal, 65, 1853–1856, https://doi.org/10.2136/SSSAJ2001.1853, 2001.

Hemingway, J. D.: rampedpyrox: open-source tools for thermoanalytical data analysis, https://doi.org/10.5281/zenodo.839815, 2016.

Hemingway, J. D., Rothman, D. H., Rosengard, S. Z., and Galy, V.: Technical note: An inverse method to relate organic carbon reactivity to isotope composition from serial oxidation, Biogeosciences, 14, 5099–5114, https://doi.org/10.5194/BG-14-5099-2017, 2017.

Hemingway, J. D., Rothman, D. H., Grant, K. E., Rosengard, S. Z., Eglinton, T. I., Derry, L. A., and Galy, V.: Mineral protection regulates long-term global preservation of natural organic carbon, Nature, 570, 228–231, https://doi.org/10.1038/s41586-019-1280-6, 2019.

Hugelius, G., Strauss, J., Zubrzycki, S., Harden, J. W., Schuur, E. A. G., Ping, C. L., Schirrmeister, L., Grosse, G., Michaelson, G. J., Koven, C. D., O'Donnell, J. A., Elberling, B., Mishra, U., Camill, P., Yu, Z., Palmtag, J., and Kuhry, P.: Estimated stocks of circumpolar permafrost carbon with quantified uncertainty ranges and identified data gaps, Biogeosciences, 11, 6573–6593, https://doi.org/10.5194/bg-11-6573-2014, 2014.

Kaal, J., Martínez Cortizas, A., and Nierop, K. G. J.: Characterisation of aged charcoal using a coil probe pyrolysis-GC/MS method optimised for black carbon, J. Anal. Appl. Pyrolysis, 85, 408–416, https://doi.org/10.1016/J.JAAP.2008.11.007, 2009.

Kaal, J., Wagner, S., and Jaffé, R.: Molecular properties of ultrafiltered dissolved organic matter and dissolved black carbon in headwater streams as determined by pyrolysis-GC/MS, J. Anal. Appl. Pyrolysis, 118, 181–191, https://doi.org/10.1016/J.JAAP.2016.02.003, 2016.

Keskitalo, K. H., Bröder, L., Shakil, S., Zolkos, S., Tank, S. E., Van Dongen, B. E., Tesi, T., Haghipour, N., Eglinton, T. I., Kokelj, S. V., and Vonk, J. E.: Downstream Evolution of Particulate Organic Matter Composition From Permafrost Thaw Slumps, Front. Earth Sci. (Lausanne)., 9, 642675, https://doi.org/10.3389/feart.2021.642675, 2021.

Knoblauch, C., Beer, C., Sosnin, A., Wagner, D., and Pfeiffer, E. -M.: Predicting long-term carbon mineralization and trace gas production from thawing permafrost of Northeast Siberia, Glob. Chang. Biol., 19, 1160–1172, https://doi.org/10.1111/gcb.12116, 2013.

Kokelj, S. V., Lacelle, D., Lantz, T. C., Tunnicliffe, J., Malone, L., Clark, I. D., and Chin, K. S.: Thawing of massive ground ice in mega slumps drives increases in stream sediment and solute flux across a range of watershed scales, J. Geophys. Res. Earth Surf., 118, 681–692, https://doi.org/10.1002/JGRF.20063, 2013.

Kokelj, S. V., Tunnicliffe, J., Lacelle, D., Lantz, T. C., Chin, K. S., and Fraser, R.: Increased precipitation drives mega slump development and destabilization of ice-rich permafrost terrain, northwestern Canada, Glob. Planet. Change, 129, 56–68, https://doi.org/10.1016/J.GLOPLACHA.2015.02.008, 2015.

Kokelj, S. V., Lantz, T. C., Tunnicliffe, J., Segal, R. A., and Lacelle, D.: Climate-driven thaw of permafrost preserved glacial landscapes, northwestern Canada, Geology, 45, 371–374, https://doi.org/10.1130/G38626.1, 2017.

Kokelj, S. V., Kokoszka, J., Van Der Sluijs, J., Rudy, A. C. A., Tunnicliffe, J., Shakil, S., Tank, S. E., and Zolkos, S.: Thaw-driven mass wasting couples slopes with downstream systems, and effects propagate through Arctic drainage networks, Cryosphere, 15, 3059–3081, https://doi.org/10.5194/TC-15-3059-2021, 2021.

Komada, T., Anderson, M. R., and Dorfmeier, C. L.: Carbonate removal from coastal sediments for the determination of organic carbon and its isotopic signatures, δ13C and Δ14C: Comparison of fumigation and direct acidification by hydrochloric acid, Limnol. Oceanogr. Methods, 6, 254–262, https://doi.org/10.4319/LOM.2008.6.254, 2008.

Lacelle, D., Fontaine, M., Pellerin, A., Kokelj, S. V., and Clark, I. D.: Legacy of Holocene Landscape Changes on Soil Biogeochemistry: A Perspective From Paleo-Active Layers in Northwestern Canada, J. Geophys. Res. Biogeosci., 124, 2662–2679, https://doi.org/10.1029/2018JG004916, 2019.

De Leeuw, J. W. and Largeau, C.: A Review of Macromolecular Organic Compounds That Comprise Living Organisms and Their Role in Kerogen, Coal, and Petroleum Formation, Organic Geochemistry: Principles and Applications, 23–72, https://doi.org/10.1007/978-1-4615-2890-6_2, 1993.

Lewis, C. A.: The kinetics of biomarker reactions: implications for the assessment of the thermal maturity of organic matter in sedimentary basins, Organic Geochemistry: Principles and Applications, 491–510, https://doi.org/10.1007/978-1-4615-2890-6_22, 1993.

Lewkowicz, A. G. and Way, R. G.: Extremes of summer climate trigger thousands of thermokarst landslides in a High Arctic environment, Nat. Commun., 10, 1–11, https://doi.org/10.1038/S41467-019-09314-7, 2019.

Littlefair, C. A., Tank, S. E., and Kokelj, S. V.: Retrogressive thaw slumps temper dissolved organic carbon delivery to streams of the Peel Plateau, NWT, Canada, Biogeosciences, 14, 5487–5505, https://doi.org/10.5194/BG-14-5487-2017, 2017.

Mann, P. J., Eglinton, T. I., McIntyre, C. P., Zimov, N., Davydova, A., Vonk, J. E., Holmes, R. M., and Spencer, R. G. M.: Utilization of ancient permafrost carbon in headwaters of Arctic fluvial networks, Nat. Commun., 6, 1–7, https://doi.org/10.1038/NCOMMS8856, 2015.

De Maria, D., Fahrni, S. M., Lozac'h, F., Marvalin, C., Walles, M., Camenisch, G., Wacker, L., and Synal, H. A.: Double Trap Interface: A novel gas interface for high throughput analysis of biomedical samples by AMS, Drug Metab. Pharmacokinet., 39, 100400, https://doi.org/10.1016/J.DMPK.2021.100400, 2021.

Martens, J., Mueller, C. W., Joshi, P., Rosinger, C., Maisch, M., Kappler, A., Bonkowski, M., Schwamborn, G., Schirrmeister, L., and Rethemeyer, J.: Stabilization of mineral-associated organic carbon in Pleistocene permafrost, Nat. Commun., 14, 2120, https://doi.org/10.1038/s41467-023-37766-5, 2023.

Mishra, U., Hugelius, G., Shelef, E., Yang, Y., Strauss, J., Lupachev, A., Harden, J. W., Jastrow, J. D., Ping, C. L., Riley, W. J., Schuur, E. A. G., Matamala, R., Siewert, M., Nave, L. E., Koven, C. D., Fuchs, M., Palmtag, J., Kuhry, P., Treat, C. C., Zubrzycki, S., Hoffman, F. M., Elberling, B., Camill, P., Veremeeva, A., and Orr, A.: Spatial heterogeneity and environmental predictors of permafrost region soil organic carbon stocks, Sci. Adv., 7, 5236–5260, https://doi.org/10.1126/SCIADV.AAZ5236, 2021.

Mittelbach, B. V. A., Brunmayr, A. S., White, M. E., Rhyner, T. M. Y., Haghipour, N., Blattmann, T. M., Wessels, M., Dubois, N., and Eglinton, T. I.: Pre-aged organic matter dominates organic carbon burial in a major perialpine lake system, Limnol. Oceanogr., 70, 911–924, https://doi.org/10.1002/LNO.12815, 2025.

Morgenstern, A., Ulrich, M., Günther, F., Roessler, S., Fedorova, I., Rudaya, N. A., Wetterich, S., Boike, J., and Schirrmeister, L.: Evolution of thermokarst in East Siberian ice-rich permafrost: A case study, Geomorphology, 201, 363–379, https://doi.org/10.1594/PANGAEA.848491, 2013.

Overland, J. E., Dunlea, E., Box, J. E., Corell, R., Forsius, M., Kattsov, V., Olsen, M. S., Pawlak, J., Reiersen, L. O., and Wang, M.: The urgency of Arctic change, Polar Sci., 21, 6–13, https://doi.org/10.1016/J.POLAR.2018.11.008, 2019.

Ping, C. L., Bockheim, J. G., Kimble, J. M., Michaelson, G. J., and Walker, D. A.: Characteristics of cryogenic soils along a latitudinal transect in Arctic Alaska, Journal of Geophysical Research: Atmospheres, 103, 28917–28928, https://doi.org/10.1029/98jd02024, 1998.

Ping, C. L., Michaelson, G. J., Jorgenson, M. T., Kimble, J. M., Epstein, H., Romanovsky, V. E., and Walker, D. A.: High stocks of soil organic carbon in the North American Arctic region, Nat. Geosci., 1, 615–619, https://doi.org/10.1038/ngeo284, 2008.

Ramage, J. L., Irrgang, A. M., Herzschuh, U., Morgenstern, A., Couture, N., and Lantuit, H.: Terrain controls on the occurrence of coastal retrogressive thaw slumps along the Yukon Coast, Canada, J. Geophys. Res. Earth Surf., 122, 1619–1634, https://doi.org/10.1002/2017JF004231, 2017.

Ramsperger, U., De Maria, D., Gautschi, P., Maxeiner, S., Müller, A. M., Synal, H. A., and Wacker, L.: Lea—a novel low energy accelerator for 14C dating, Radiocarbon, 66, 1280–1288, https://doi.org/10.1017/RDC.2023.85, 2024.

Rantanen, M., Karpechko, A. Y., Lipponen, A., Nordling, K., Hyvärinen, O., Ruosteenoja, K., Vihma, T., and Laaksonen, A.: The Arctic has warmed nearly four times faster than the globe since 1979, Commun. Earth Environ., 3, 1–10, https://doi.org/10.1038/s43247-022-00498-3, 2022.

Reimer, P. J., Brown, T. A., and Reimer, R. W.: Discussion: Reporting and Calibration of Post-Bomb 14C Data, Radiocarbon, 46, 1299–1304, https://doi.org/10.1017/S0033822200033154, 2004.

Reimer, P. J., Austin, W. E. N., Bard, E., Bayliss, A., Blackwell, P. G., Bronk Ramsey, C., Butzin, M., Cheng, H., Edwards, R. L., Friedrich, M., Grootes, P. M., Guilderson, T. P., Hajdas, I., Heaton, T. J., Hogg, A. G., Hughen, K. A., Kromer, B., Manning, S. W., Muscheler, R., Palmer, J. G., Pearson, C., Van Der Plicht, J., Reimer, R. W., Richards, D. A., Scott, E. M., Southon, J. R., Turney, C. S. M., Wacker, L., Adolphi, F., Büntgen, U., Capano, M., Fahrni, S. M., Fogtmann-Schulz, A., Friedrich, R., Köhler, P., Kudsk, S., Miyake, F., Olsen, J., Reinig, F., Sakamoto, M., Sookdeo, A., and Talamo, S.: The IntCal20

Northern Hemisphere Radiocarbon Age Calibration Curve (0-55 cal kBP), Radiocarbon, 62, 725–757, https://doi.org/10.1017/RDC.2020.41, 2020.

Schädel, C., Schuur, E. A. G., Bracho, R., Elberling, B., Knoblauch, C., Lee, H., Luo, Y., Shaver, G. R., and Turetsky, M. R.: Circumpolar assessment of permafrost C quality and its vulnerability over time using long-term incubation data, Glob. Chang. Biol., 20, 641–652, https://doi.org/10.1111/GCB.12417, 2014.

Schnitzer, M. and Monreal, C. M.: Quo Vadis Soil Organic Matter Research? A Biological Link to the Chemistry of Humification, Advances in Agronomy, 113, 143–217, https://doi.org/10.1016/B978-0-12-386473-4.00003-8, 2011.

Schuur, E. A. G., Bockheim, J. G., Canadell, J. G., Euskirchen, E., Field, C. B., Goryachkin, S. V., Hagemann, S., Kuhry, P., Lafleur, P. M., Lee, H., Mazhitova, G., Nelson, F. E., Rinke, A., Romanovsky, V. E., Shiklomanov, N., Tarnocai, C., Venevsky, S., Vogel, J. G., and Zimov, S. A.: Vulnerability of Permafrost Carbon to Climate Change: Implications for the Global Carbon Cycle, Bioscience, 58, 701–714, https://doi.org/10.1641/B580807, 2008.

Schuur, E. A. G., McGuire, A. D., Schädel, C., Grosse, G., Harden, J. W., Hayes, D. J., Hugelius, G., Koven, C. D., Kuhry, P., Lawrence, D. M., Natali, S. M., Olefeldt, D., Romanovsky, V. E., Schaefer, K., Turetsky, M. R., Treat, C. C., and Vonk, J. E.: Climate change and the permafrost carbon feedback, Nature, 520, 171–179, https://doi.org/10.1038/nature14338, 2015.

Segal, R. A., Lantz, T. C., and Kokelj, S. V.: Acceleration of thaw slump activity in glaciated landscapes of the Western Canadian Arctic, Environmental Research Letters, 11, 034025, https://doi.org/10.1088/1748-9326/11/3/034025, 2016a.

Segal, R. A., Lantz, T. C., and Kokelj, S. V.: Acceleration of thaw slump activity in glaciated landscapes of the Western Canadian Arctic, Environmental Research Letters, 11, 034025, https://doi.org/10.1088/1748-9326/11/3/034025, 2016b.

Shakil, S., Tank, S. E., Kokelj, S. V., Vonk, J. E., and Zolkos, S.: Particulate dominance of organic carbon mobilization from thaw slumps on the Peel Plateau, NT: Quantification and implications for stream systems and permafrost carbon release, Environmental Research Letters, 15, 114019, https://doi.org/10.1088/1748-9326/ABAC36, 2020.

Shakil, S., Tank, S. E., Vonk, J. E., and Zolkos, S.: Low biodegradability of particulate organic carbon mobilized from thaw slumps on the Peel Plateau, NT, and possible chemosynthesis and sorption effects, Biogeosciences, 19, 1871–1890, https://doi.org/10.5194/BG-19-1871-2022, 2022.

Stoner, S. W., Schrumpf, M., Hoyt, A., Sierra, C. A., Doetterl, S., Galy, V., and Trumbore, S.: How well does ramped thermal oxidation quantify the age distribution of soil carbon? Assessing thermal stability of physically and chemically fractionated soil organic matter, Biogeosciences, 20, 3151–3163, https://doi.org/10.5194/egusphere-2022-624, 2023.

Strauss, J., Schirrmeister, L., Grosse, G., Fortier, D., Hugelius, G., Knoblauch, C., Romanovsky, V., Schädel, C., Schneider von Deimling, T., Schuur, E. A. G., Shmelev, D., Ulrich, M., and Veremeeva, A.: Deep Yedoma permafrost: A synthesis of depositional characteristics and carbon vulnerability, Earth. Sci. Rev., 172, 75–86, https://doi.org/10.1016/J.EARSCIREV.2017.07.007, 2017.

Strauss, J., Fuchs, M., Hugelius, G., Miesner, F., Nitze, I., Opfergelt, S., Schuur, E., Treat, C. C., Turetsky, M., Yang, Y., and Grosse, G.: Organic matter storage and vulnerability in the permafrost domain, Encyclopedia of Quaternary Science, 399–410, https://doi.org/10.1016/B978-0-323-99931-1.00164-1, 2025.

Stuiver, M. and Polach, H. A.: Discussion Reporting of 14C Data, Radiocarbon, 19, 355–363, https://doi.org/10.1017/S0033822200003672, 1977.

Synal, H. A., Stocker, M., and Suter, M.: MICADAS: a new compact radiocarbon AMS system, Nucl. Instrum. Methods Phys. Res. B, 259, 7–13, https://doi.org/10.1016/j.nimb.2007.01.138, 2007.

Thomas, M., Monhonval, A., Hirst, C., Bröder, L., Zolkos, S., Vonk, J. E., Tank, S. E., Keskitalo, K. H., Shakil, S., Kokelj, S. V., van der Sluijs, J., and Opfergelt, S.: Evidence for preservation of organic carbon interacting with iron in material displaced from retrogressive thaw slumps: Case study in Peel Plateau, western Canadian Arctic, Geoderma, 433, 116443, https://doi.org/10.1016/J.GEODERMA.2023.116443, 2023.

Tolu, J., Gerber, L., Boily, J. F., and Bindler, R.: High-throughput characterization of sediment organic matter by pyrolysis–gas chromatography/mass spectrometry and multivariate curve resolution: A promising analytical tool in (paleo)limnology, Anal. Chim. Acta, 880, 93–102, https://doi.org/10.1016/J.ACA.2015.03.043, 2015.

Vaughn, L. J. S. and Torn, M. S.: 14C evidence that millennial and fast-cycling soil carbon are equally sensitive to warming, Nat. Clim. Chang., 9, 467–471, https://doi.org/10.1038/s41558-019-0468-y, 2019.

Vonk, J. E., Mann, P. J., Davydov, S., Davydova, A., Spencer, R. G. M., Schade, J., Sobczak, W. V., Zimov, N., Zimov, S., Bulygina, E., Eglinton, T. I., and Holmes, R. M.: High biolability of ancient permafrost carbon upon thaw, Geophys. Res. Lett., 40, 2689–2693, https://doi.org/10.1002/grl.50348, 2013.

Vonk, J. E., Giosan, L., Blusztajn, J., Montlucon, D., Graf Pannatier, E., McIntyre, C., Wacker, L., Macdonald, R. W., Yunker, M. B., and Eglinton, T. I.: Spatial variations in geochemical characteristics of the modern Mackenzie Delta sedimentary system, Geochim. Cosmochim. Acta, 171, 100–120, https://doi.org/10.1016/J.GCA.2015.08.005, 2015.

Wenig, P. and Odermatt, J.: OpenChrom: A cross-platform open source software for the mass spectrometric analysis of chromatographic data, BMC Bioinformatics, 11, 1–9, https://doi.org/10.1186/1471-2105-11-405, 2010.

Zaccone, C., Sanei, H., Outridge, P. M., and Miano, T. M.: Studying the humification degree and evolution of peat down a Holocene bog profile (Inuvik, NW Canada): A petrological and chemical perspective, Org. Geochem., 42, 399–408, https://doi.org/10.1016/j.orggeochem.2011.02.004, 2011.

Zolkos, S., Tank, S. E., and Kokelj, S. V.: Mineral Weathering and the Permafrost Carbon-Climate Feedback, Geophys. Res. Lett., 45, 9623–9632, https://doi.org/10.1029/2018GL078748, 2018.

Zolkos, S., Tank, S. E., Striegl, R. G., and Kokelj, S. V.: Thermokarst Effects on Carbon Dioxide and Methane Fluxes in Streams on the Peel Plateau (NWT, Canada), J. Geophys. Res. Biogeosci., 124, 1781–1798, https://doi.org/10.1029/2019JG005038, 2019.

Supplementary material – In-depth characterisation of organic matter lability and composition from Arctic Permafrost thaw slumps

Marco A. Bolandini[1], Negar Haghipour[1,2], Kirsi H. Keskitalo[4], Jorien E. Vonk[3], Jordon D. Hemingway[1], Timothy I. Eglinton[1], Lisa Bröder[1]

[1]Geological Institute, Department of Earth and Planetary Sciences, ETH Zurich, Sonneggstrasse 5, 8092 Zurich, Switzerland
[2]Laboratory for Ion Beam Physics, Department of Physics, ETH Zurich, Otto-Stern-Weg 5, 8093 Zurich, Switzerland
[3]Earth and Climate, Faculty of Science, Vrije Universiteit Amsterdam, De Boelelaan 1085, 1081 HV Amsterdam, Netherlands
[4]School of Geography and Natural Sciences, Northumbria University, Ellison Place, Newcastle upon Tyne UK-NE1 8ST, United Kingdom

Correspondence to: Marco A. Bolandini (marcobo@eaps.ethz.ch)

Supplementary material

Supplementary tables

Table S1. Summary of integrated thermal stability and radiocarbon parameters for each sample. Columns show: sample name, maximum activation energy (E_{max}, kJ mol^{-1}), mean activation energy (E_{mean}, kJ mol^{-1}) with standard deviation (± kJ mol^{-1}), maximum probability density $p_0(E)$, residual oxidisable carbon to total organic carbon ratio (ROC/TOC, %), threshold temperature for ROC/TOC (°C), estimated mass of ROC carbon (µg), weighted fraction modern radiocarbon ($F^{14}C$) with standard deviation (±), total carbon mass (µg), and associated mass error (± µg).

Sample Name	E_max (kJ/mol)	E_mean (kJ/mol)	E_std (kJ/mol)	p0(E)_max	ROC/TOC (%)	Threshold ROC/TOC Temperature (°C)	Estimated ROC Carbon (µg)	Weighted $F^{14}C$	$F^{14}C$ std (±)	Total Carbon Mass (µg)	Total Mass Error (± µg)
Fm2_AL	158.271	151.802	17.086	0.027	4.300	477.000	53.877	0.704	0.009	1252.964	31.716
Fm2_HO1	156.015	165.165	20.700	0.022	33.100	441.100	155.063	0.120	0.007	468.467	11.858
Fm2_HO2	160.526	161.850	17.133	0.029	31.900	417.900	197.858	0.072	0.006	620.243	15.700
Fm2_PL	152.256	162.963	19.731	0.022	38.200	413.300	261.191	0.021	0.005	683.745	17.308
Fm2_RU	156.767	166.908	19.913	0.019	40.300	429.200	214.926	0.115	0.007	533.314	13.500
Fm3_AL2	172.556	151.955	21.151	0.021	14.600	451.600	148.104	0.333	0.008	1014.414	25.678
Fm3_AL3	140.226	155.535	23.718	0.017	31.700	406.000	167.240	0.282	0.008	527.571	13.354
Fm3_HO	162.030	170.921	24.275	0.019	36.400	438.700	203.082	0.036	0.005	557.917	14.123
Fm3_DB	160.526	168.637	22.510	0.020	38.700	428.500	189.067	0.039	0.005	488.546	12.367
Fm3_RU	156.767	166.908	19.913	0.019	35.600	419.000	227.568	0.049	0.005	639.237	16.181

Table S2. Bulk carbon composition of each sample. Columns show sample name, total sample weight (mg), total carbon content (TC, %), total organic carbon (TOC, %), total inorganic carbon released at 900 °C (TIC, %), organic carbon released at 400 °C (TOC_{400}, %), and residual oxidisable carbon (ROC, %).

Name	Weigh (mg)	TC (%)	TOC (%)	TIC (%)
Fm2 AL	31.500	16.646	16.297	0.349
Fm2 HO1	79.700	1.143	1.028	0.115
Fm2 HO2	64.800	1.114	0.984	0.131
Fm2 PL	54.100	1.404	1.252	0.152
Fm2 RU	55.600	1.473	1.304	0.168
Fm3 AL2	40.300	7.575	7.276	0.299
Fm3 AL3	39.900	3.691	3.411	0.280
Fm3 HO	61.700	1.297	1.153	0.144
Fm3 DB	61.600	1.301	1.158	0.144
Fm3 RU	64.200	1.585	1.439	0.146
CB_AL1	40.200	1.857	1.646	0.210
CB_AL2	44.000	3.708	3.499	0.209
CB_AL3	45.700	2.700	2.500	0.200
CB_AL4	41.600	2.094	1.880	0.215
CB_HO	64.600	1.316	1.174	0.142
CB_DB	55.400	1.656	1.499	0.157
CB_RU	59.200	1.569	1.422	0.147
SF_AL	59.500	1.952	1.793	0.159
SF_HO	60.400	1.444	1.291	0.153
SF_DB	72.900	1.262	1.139	0.123
SF_RU	60.300	1.495	1.349	0.146

Table S3. Summary of ORO–AMS measurements for all samples and thermal windows. Columns show: sample ID, thermal window (°C), oxidation start time (t_0, s), oxidation end time (t_f, s), carbon mass released per thermal window (µg) with associated uncertainty (± µg), fraction modern radiocarbon ($F^{14}C$) with standard deviation (±), proportional contribution to total carbon release (fraction), mean activation energy (*E*, kJ mol^{-1}) with standard deviation (± kJ mol^{-1}), and stable carbon isotope composition ($\delta^{13}C$, ‰).

Sample	Temperature Window (°C)	t0 (s)	tf (s)	Mass thermal window (µg)	Mass error (± µg)	$F^{14}C$	$F^{14}C$ std (±)	fraction	E (kJ/mol)	E std. (± kJ/mol)
Fm2_AL	150-240	1385	2532	74.891	1.896	0.725	0.008	1	124	6
Fm2_AL	240-300	2533	3435	251.496	6.366	0.713	0.008	2	134	7
Fm2_AL	300-350	3436	4189	282.838	7.159	0.672	0.008	3	146	7
Fm2_AL	350-400	4190	4955	339.519	8.594	0.708	0.008	4	158	6
Fm2_AL	400-455	4956	5793	207.709	5.258	0.729	0.008	5	167	7
Fm2_AL	455-510	5794	6632	76.437	1.935	0.699	0.007	6	180	6
Fm2_AL	510-600	6633	8023	20.073	0.508	0.625	0.007	7	195	8
Fm2_AL	600-900	8024	10031	0.457	0.012	NA	NA	8	205	2
Fm2_HO1	150-240	1359	2508	5.074	0.128	0.262	0.005	1	130	6
Fm2_HO1	240-300	2509	3414	48.510	1.228	0.205	0.004	2	136	7
Fm2_HO1	300-350	3415	4179	88.143	2.231	0.139	0.003	3	147	7
Fm2_HO1	350-400	4180	4935	105.293	2.665	0.107	0.003	4	157	7
Fm2_HO1	400-455	4936	5772	84.113	2.129	0.096	0.003	5	171	9
Fm2_HO1	455-510	5773	6614	77.528	1.962	0.091	0.003	6	184	7
Fm2_HO1	510-600	6615	8009	59.805	1.514	0.102	0.004	7	197	7
Fm2_HO1	600-900	8010	9824	3.061	0.078	NA	NA	8	208	3
Fm2_HO2	150-240	1358	2485	4.287	0.109	0.209	0.005	1	132	6
Fm2_HO2	240-300	2486	3401	59.748	1.512	0.127	0.004	2	137	7
Fm2_HO2	300-350	3402	4154	119.813	3.033	0.079	0.003	3	148	7
Fm2_HO2	350-400	4155	4919	179.549	4.545	0.042	0.002	4	158	6
Fm2_HO2	400-455	4920	5758	137.144	3.472	0.052	0.002	5	168	7
Fm2_HO2	455-510	5759	6598	75.094	1.901	0.088	0.003	6	184	7
Fm2_HO2	510-600	6599	8007	44.609	1.129	0.123	0.004	7	194	6
Fm2_HO2	600-900	8008	10787	0.137	0.004	NA	NA	8	204	2
Fm2_PL	150-240	1468	2606	8.994	0.228	0.105	0.003	1	129	6
Fm2_PL	240-300	2607	3517	76.160	1.928	0.045	0.002	2	136	7
Fm2_PL	300-350	3518	4261	138.081	3.495	0.021	0.002	3	147	7
Fm2_PL	350-400	4262	5022	160.359	4.059	0.016	0.001	4	157	7
Fm2_PL	400-455	5023	5867	123.992	3.139	0.015	0.001	5	171	8
Fm2_PL	455-510	5868	6721	108.077	2.736	0.012	0.001	6	184	7
Fm2_PL	510-600	6722	8112	68.081	1.723	0.021	0.001	7	195	7
Fm2_PL	600-900	8113	10365	1.625	0.041	NA	NA	8	206	3
Fm2_RU	150-240	1472	2601	3.575	0.091	0.239	0.006	1	132	6
Fm2_RU	240-300	2602	3500	45.649	1.156	0.192	0.004	2	137	7
Fm2_RU	300-350	3501	4278	92.559	2.343	0.131	0.003	3	147	7
Fm2_RU	350-400	4279	5036	111.741	2.829	0.108	0.003	4	158	7
Fm2_RU	400-455	5037	5876	114.933	2.909	0.093	0.003	5	171	8
Fm2_RU	455-510	5877	6717	99.387	2.516	0.106	0.003	6	183	7
Fm2_RU	510-600	6718	8108	65.469	1.657	0.097	0.003	7	197	8
Fm2_RU	600-900	8109	10204	4.611	0.117	NA	NA	8	210	4

Sample	Temperature Window (°C)	t0 (s)	tf (s)	Mass thermal window (µg)	Mass error (± µg)	$F^{14}C$	$F^{14}C$ std (±)	fraction	E (kJ/mol)	E std. (± kJ/mol)
Fm3_AL2	150-240	1566	2702	106.600	2.698	0.337	0.005	1	121	6
Fm3_AL2	240-300	2703	3614	231.053	5.849	0.339	0.007	2	133	7
Fm3_AL2	300-350	3615	4367	188.344	4.768	0.324	0.006	3	145	7
Fm3_AL2	350-400	4368	5135	144.903	3.668	0.329	0.006	4	159	9
Fm3_AL2	400-455	5136	5966	203.368	5.148	0.341	0.005	5	171	6
Fm3_AL2	455-510	5967	6819	113.911	2.883	0.328	0.005	6	179	6
Fm3_AL2	510-600	6820	8255	26.235	0.664	0.327	0.006	7	193	6
Fm3_AL2	600-900	NA	NA	0.000	0.000	NA	NA	8	0	0
Fm3_AL3	150-240	1485	2625	43.726	1.107	0.309	0.006	1	122	7
Fm3_AL3	240-300	2626	3536	112.809	2.856	0.294	0.005	2	133	7
Fm3_AL3	300-350	3537	4291	101.437	2.568	0.268	0.005	3	145	7
Fm3_AL3	350-400	4292	5056	85.077	2.154	0.295	0.005	4	158	8
Fm3_AL3	400-455	5057	5897	90.473	2.290	0.271	0.005	5	171	7
Fm3_AL3	455-510	5898	6739	61.264	1.551	0.272	0.005	6	182	7
Fm3_AL3	510-600	6740	8055	32.785	0.830	0.267	0.007	7	197	8
Fm3_AL3	600-900	8056	9690	7.877	0.199	NA	NA	8	222	10
Fm3_HO	150-240	1714	2840	5.925	0.150	0.106	0.004	1	129	6
Fm3_HO	240-300	2841	3763	49.912	1.263	0.074	0.003	2	136	7
Fm3_HO	300-350	3764	4513	87.868	2.224	0.049	0.002	3	147	7
Fm3_HO	350-400	4514	5267	112.679	2.852	0.038	0.002	4	158	7
Fm3_HO	400-455	5268	6111	108.595	2.749	0.031	0.002	5	170	8
Fm3_HO	455-510	6112	6958	92.931	2.352	0.017	0.002	6	185	8
Fm3_HO	510-600	6959	8341	100.007	2.531	0.023	0.002	7	199	8
Fm3_HO	600-900	8342	10665	26.833	0.679	NA	NA	8	223	13
Fm3_DB	150-240	1558	2703	4.864	0.123	0.133	0.004	1	130	6
Fm3_DB	240-300	2704	3595	43.497	1.101	0.084	0.003	2	136	7
Fm3_DB	300-350	3596	4356	82.889	2.098	0.050	0.002	3	147	7
Fm3_DB	350-400	4357	5119	105.309	2.666	0.038	0.002	4	158	7
Fm3_DB	400-455	5120	5957	94.050	2.381	0.028	0.002	5	170	8
Fm3_DB	455-510	5958	6806	80.504	2.038	0.024	0.002	6	185	8
Fm3_DB	510-600	6807	8193	77.433	1.960	0.025	0.002	7	198	8
Fm3_DB	600-900	8194	10508	13.925	0.352	NA	NA	8	218	11
Fm3_RU	150-240	1424	2564	15.129	0.383	0.116	0.003	1	126	6
Fm3_RU	240-300	2565	3481	82.297	2.083	0.071	0.003	2	135	7
Fm3_RU	300-350	3482	4241	128.834	3.261	0.050	0.003	3	147	7
Fm3_RU	350-400	4242	4987	137.515	3.481	0.043	0.002	4	157	7
Fm3_RU	400-455	4988	5833	112.279	2.842	0.043	0.002	5	171	8
Fm3_RU	455-510	5834	6677	98.011	2.481	0.042	0.002	6	183	7
Fm3_RU	510-600	6678	8065	65.172	1.650	0.041	0.002	7	197	8
Fm3_RU	600-900	8066	10379	7.000	0.177	NA	NA	8	215	11

Table S4. Summary of identified peaks from Py–GCMS analyses across thermal windows (150–850 °C) for Fm2 and Fm3 samples. See separate file PyroGCMS_Fm2_Fm3_150_850.csv. Columns include Source File, Sample, Peak Number, Retention Time, Peak Area, Peak Area [%], Target (OpenChrom identification), and Classifier (compound group).

Supplementary figures

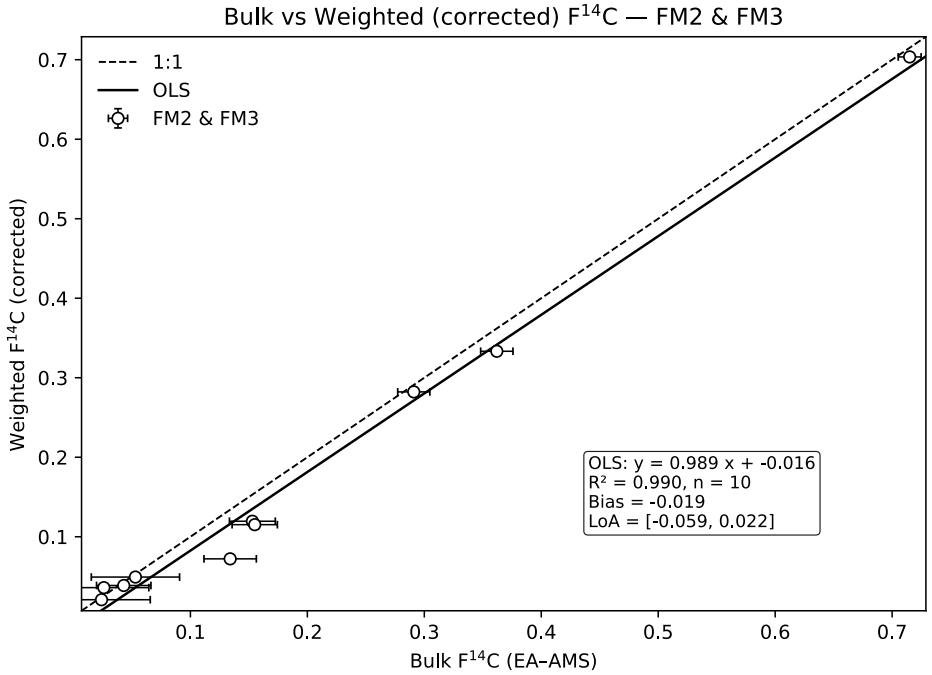

Figure S1. Comparison between thermally integrated (weighted) and bulk F¹⁴C values for thaw-slump samples from FM2 and FM3 both in circles Bulk F14C were taken from Bröder et al. (2021). The 1:1 line (grey dashed) marks perfect agreement. Weighted values closely reproduce bulk F¹⁴C measurements (OLS = 0.989 x – 0.016; R^2 = 0.99), confirming that the thermal integration approach captures the bulk radiocarbon signal within analytical uncertainty.

Comparison of ROC/TOC ratios derived from SoliTOC and ORO–AMS reveals consistent trends across geomorphic features, validating the use of this metric for assessing OM thermal stability. In both datasets, PF, DB, and RU samples exhibit moderate

to high ROC/TOC values, indicating a dominance of thermally resistant carbon in remobilised and permafrost compartments. In contrast, AL samples — especially from FM2 — display lower ROC/TOC ratios (e.g., 0.24 for SoliTOC and 0.12 for ORO–AMS), reflecting greater contributions from labile and biologically active OM. While absolute values differ, typically with ORO–AMS reporting slightly lower ROC/TOC ratios, the relative order remains consistent across sites. The difference arises because ORO–AMS resolves oxidation continuously across the thermal spectrum, whereas SoliTOC defines discrete temperature intervals. This finer resolution leads to what was previously described as “more granular thermal fractionation,” meaning that ORO–AMS captures partial oxidation within the 400 °C boundary rather than assigning all remaining carbon above this point to the ROC fraction.

The coherence between these two independent methods therefore primarily demonstrates analytical comparability — that carbon oxidised below 400 °C in one system tends to do so in the other — rather than implying direct geomorphic control.

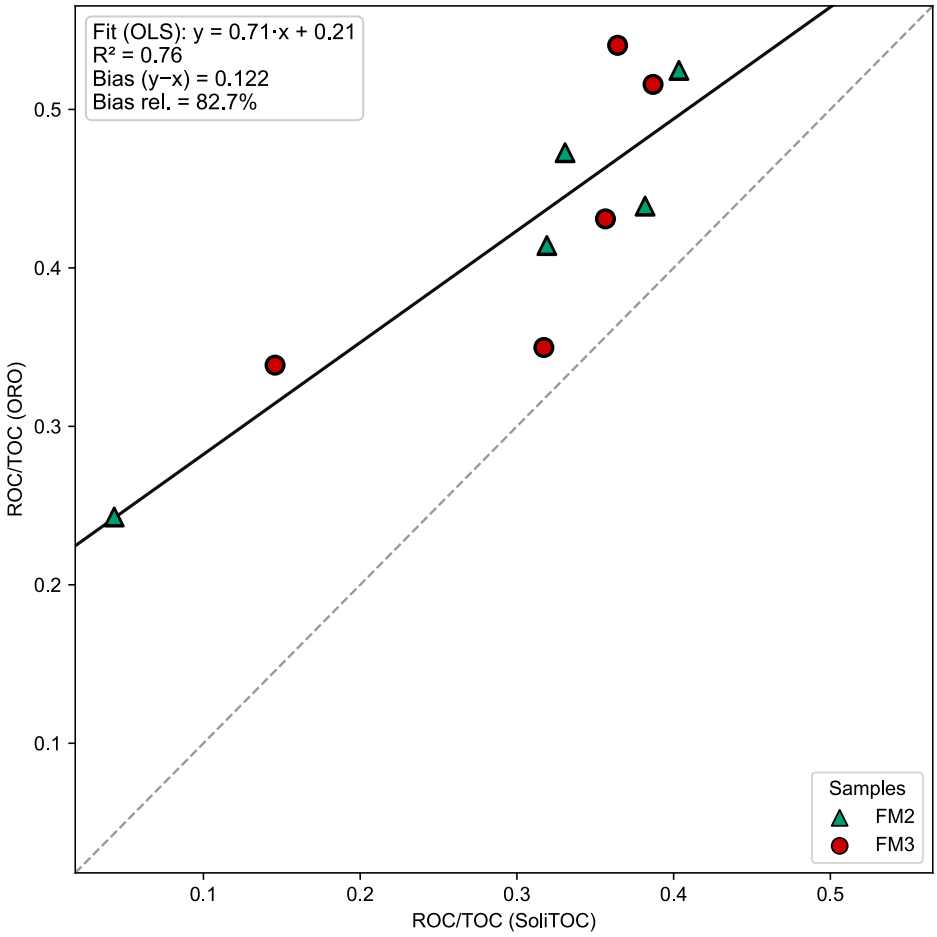

Figure S2. Cross-plot comparison of ROC/TOC ratios obtained from SoliTOC and ORO–AMS analyses for thaw-slump samples from FM2 (green triangles) and FM3 (red circles). The 1:1 line (grey dashed) indicates perfect agreement. A consistent offset is observed, with ORO–AMS reporting systematically higher ROC/TOC values (slope = 0.71, R^2 = 0.76, bias ≈ 0.12), reflecting methodological differences between continuous and stepped combustion.

Deleted: red

Deleted: slightly

Deleted: lower

However, when interpreted together with thermogram and molecular data, the pattern still supports a geomorphic gradient in OM reactivity: thermally stable carbon accumulates in PF, DB, and RU, while the AL retains fresher, more reactive OM influenced by vegetation cover, thaw depth, and cryogenic disturbance. Differences in absolute ROC/TOC ratios between SoliTOC and ORO–AMS are largely methodological. The continuous ramping approach of ORO–AMS and the discrete temperature steps of SoliTOC partition intermediate thermal fractions differently, leading to systematic offsets in ROC/TOC values. In particular, intermediate-temperature carbon fractions may be assigned differently between methods, resulting in higher apparent ROC/TOC values in ORO–AMS compared to SoliTOC. This offset (~0.2 on average in our dataset) is consistent with inter-method differences reported in similar comparative studies. These method-inherent biases highlight the value of using multiple thermal approaches to constrain OM reactivity and underscore the complementarity of SoliTOC and ORO–AMS.

Deleted: Differences in absolute ROC/TOC ratios between SoliTOC and ORO–AMS are largely methodological. SoliTOC may overestimate ROC because any carbon not oxidised at 400 °C is, by definition, considered recalcitrant — even if some of that material would combust at slightly higher, still labile, temperatures (e.g., 420–480 °C) (Natali et al., 2020; Stoner et al., 2023). By grouping such intermediate fractions into the ROC pool, SoliTOC inflates the proportion of "recalcitrant" carbon. Conversely, ORO–AMS may underestimate ROC/TOC because its continuous ramping design assigns part of this intermediate carbon to lower temperature windows, reducing the apparent size of the ROC pool. This systematic offset (~0.2 on average in our dataset) is consistent with inter-method differences reported in similar comparative studies. These method-inherent biases highlight the value of using more than one thermal approach for constraining OM reactivity and underscore the complementarity of SoliTOC and ORO–AMS.

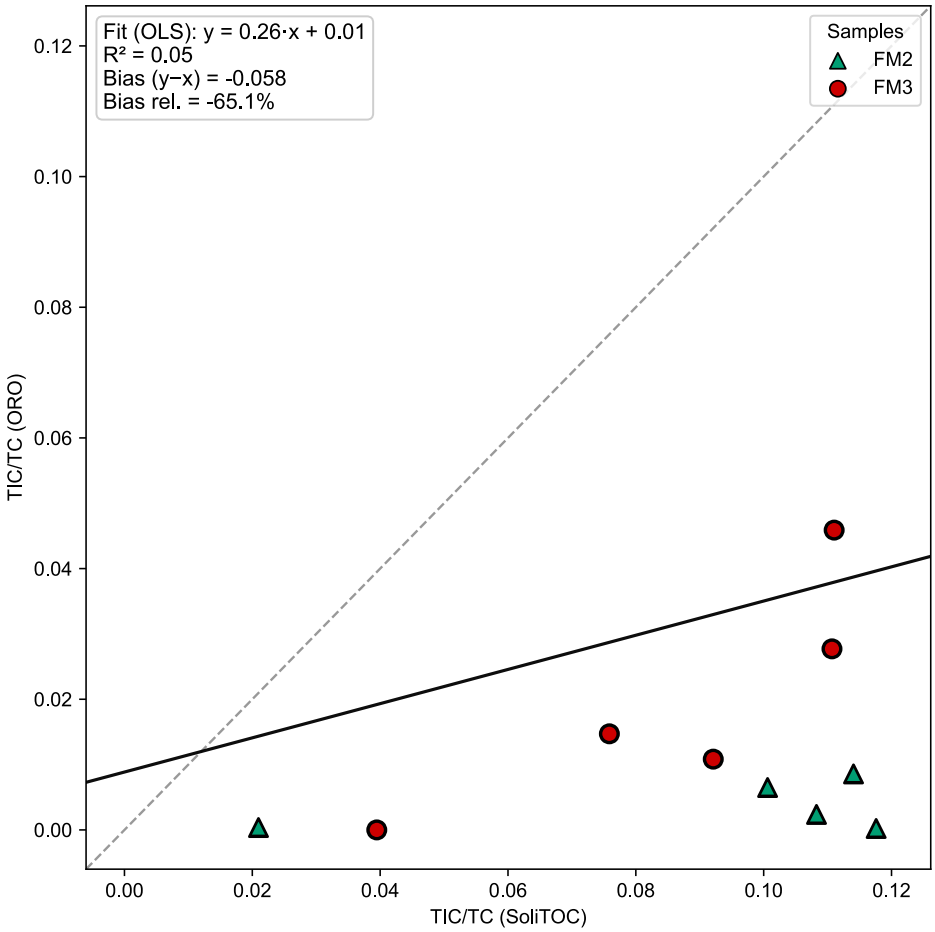

Figure S3. Cross-plot comparison of TIC/TC ratios obtained from SoliTOC and ORO analyses for thaw-slump samples from FM2 (green triangles) and FM3 (red circles). The 1:1 line (grey dashed) marks perfect agreement. Values show large scatter and no systematic 1:1 relationship (slope = 0.26, R^2 = 0.05, bias ≈ -65.1), indicating that TIC/TC is highly method-dependent. This reflects the very small carbon fraction oxidised >900 °C and differences in operational temperature windows, integration procedures, and instrument sensitivity between SoliTOC and ORO.

The two metrics show poor agreement and substantial scatter relative to the 1:1 line, with a systematic tendency for ORO to yield lower TIC/TC values than SoliTOC. This directional bias reflects fundamental differences in how carbonate decomposition is achieved by the two instruments. SoliTOC relies on fixed isothermal holds between 600 and 900 °C, during which some high-temperature carbonates (e.g. Mg-rich or Fe-bearing phases) may not fully decompose, leading to underestimation of TIC. In contrast, ORO applies continuous high-temperature oxidation under pure O_2, which more completely decomposes residual carbonates and produces larger TIC signals.

Deleted: higher

Superimposed on this directional offset is substantial scatter. Because TIC represents <1 % of total carbon after acidification, small variations in CO_2 yield, baseline subtraction, or signal integration translate into large relative differences when expressed as TIC/TC. The ORO detection chain is also more sensitive to minor adsorption, leaks, or memory effects than SoliTOC's direct TGA–IR configuration, further amplifying variability in this tail fraction. Together, these effects demonstrate that TIC/TC is strongly method-dependent and unsuitable for quantitative cross-method comparison.

By comparison, total organic carbon (TOC) measured by SoliTOC closely matches independently measured OC from elemental analysis (EA) (Fig. S4; $R^2 = 0.99$, slope = 1.00), confirming robust bulk carbon quantification. Total carbon estimates derived from ORO–AMS are also comparable to EA-OC values (Table S3), although agreement is less systematic because ORO-based values rely on mg-precision mass determination rather than direct carbon quantification. Consequently, inter-method interpretation is restricted to the more robust operational fractions (TOC_{400} and ROC), which show consistent behaviour across techniques.

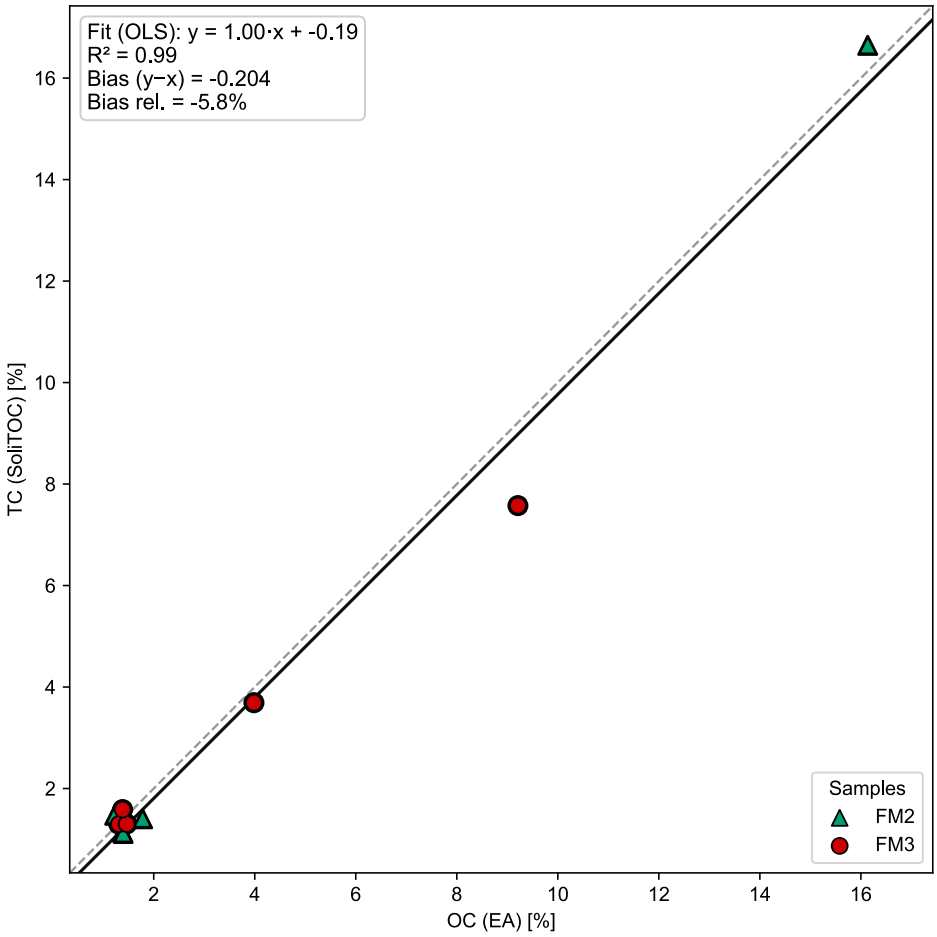

Figure S4. Cross-plot comparison of TC measured by SoliTOC and OC measured by elemental analysis (EA) for thaw-slump samples (Bröder et al., 2021) from FM2 (green triangles) and FM3 (red circles). The 1:1 line (grey dashed) indicates perfect agreement. TC and OC(EA) show near-identical values across samples (slope = 1.00, R^2 = 0.99, bias ≈ −0.20), confirming that

SoliTOC-derived total carbon closely matches independent EA-OC measurements after acidification and indicating robust quantification of the bulk organic carbon pool.

To verify the consistency of total organic carbon quantification across independent analytical methods, we compared TC values from SoliTOC with OC measurements obtained via elemental analysis (EA). All samples were acidified prior to both analyses, ensuring that measured carbon corresponds to organic carbon. The cross-plot (Fig. S4) shows excellent agreement between the two methods, with all samples falling close to the 1:1 line and a regression slope of ~1.00 ($R^2 = 0.99$). The small absolute bias (≈ −0.20 %) indicates slightly lower TC values from SoliTOC relative to EA, but the deviation is within expected analytical uncertainty for low-mass permafrost samples. This strong correspondence demonstrates that SoliTOC reliably quantifies bulk organic carbon, and that downstream ratios (TOC_{400}/TOC, ROC/TOC) are not affected by methodological inconsistencies in total-carbon estimation.

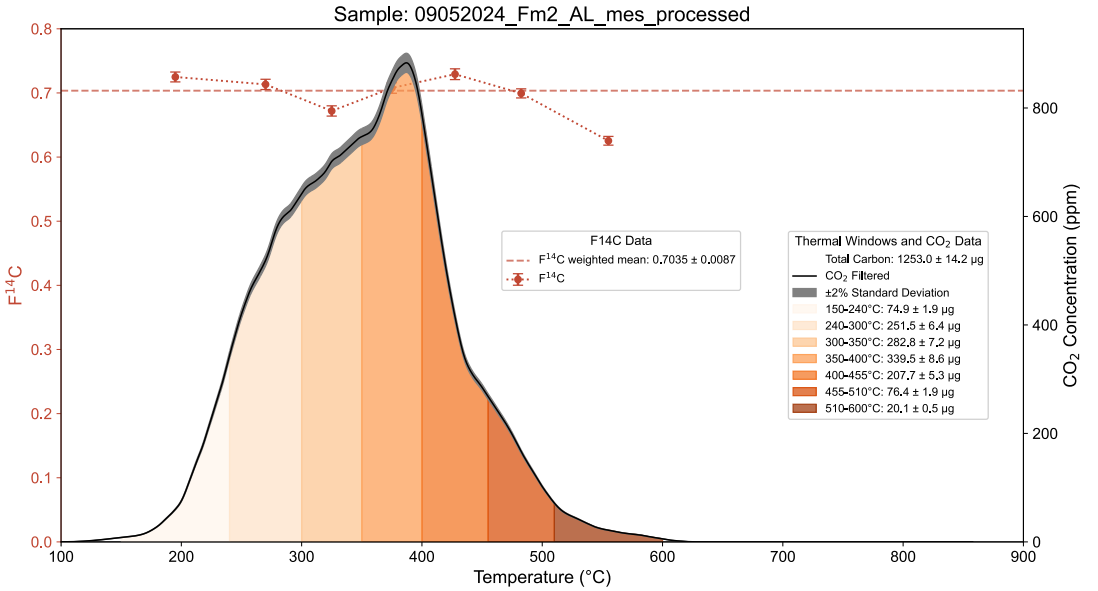

Figures S5. Thermogram of FM2-AL shows CO_2 release as a function of temperature for each sample, overlaid with corresponding $F^{14}C$ values across defined thermal windows. For each thermal window, the legends show the calculated carbon mass released (with associated error), the mass fraction (%), and the weighted $F^{14}C$ (with standard deviation). These data illustrate the relationship between carbon release dynamics, radiocarbon content, and the distribution of mass across the thermal profile.

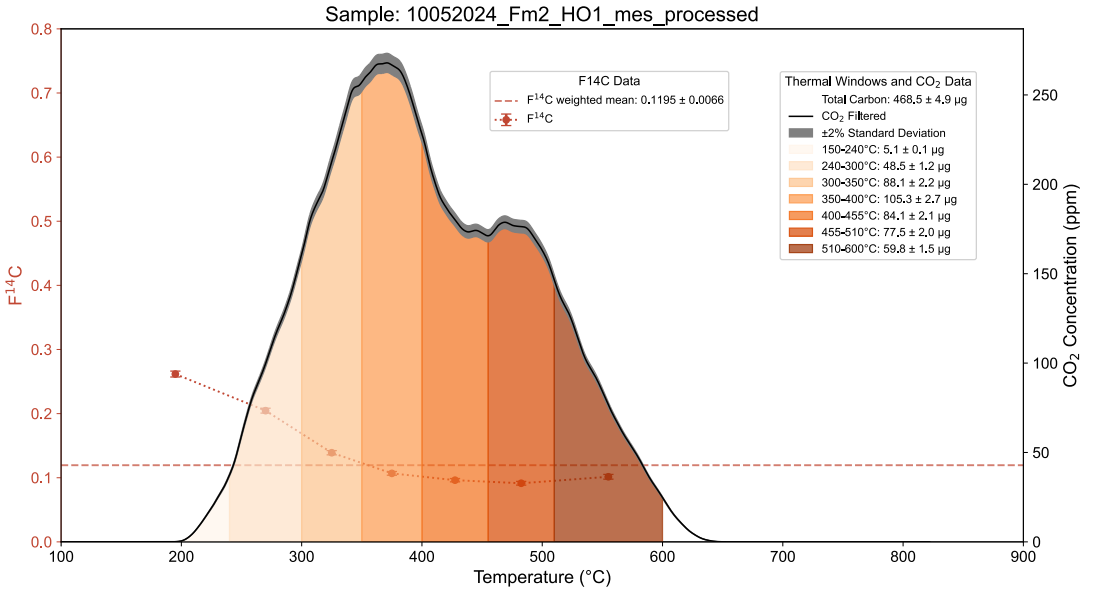

Figures S6. Thermogram of FM2-HO1 shows CO_2 release as a function of temperature for each sample, overlaid with corresponding $F^{14}C$ values across defined thermal windows. For each thermal window, the legends show the calculated carbon mass released (with associated error), the mass fraction (%), and the weighted $F^{14}C$ (with standard deviation). These data illustrate the relationship between carbon release dynamics, radiocarbon content, and the distribution of mass across the thermal profile.

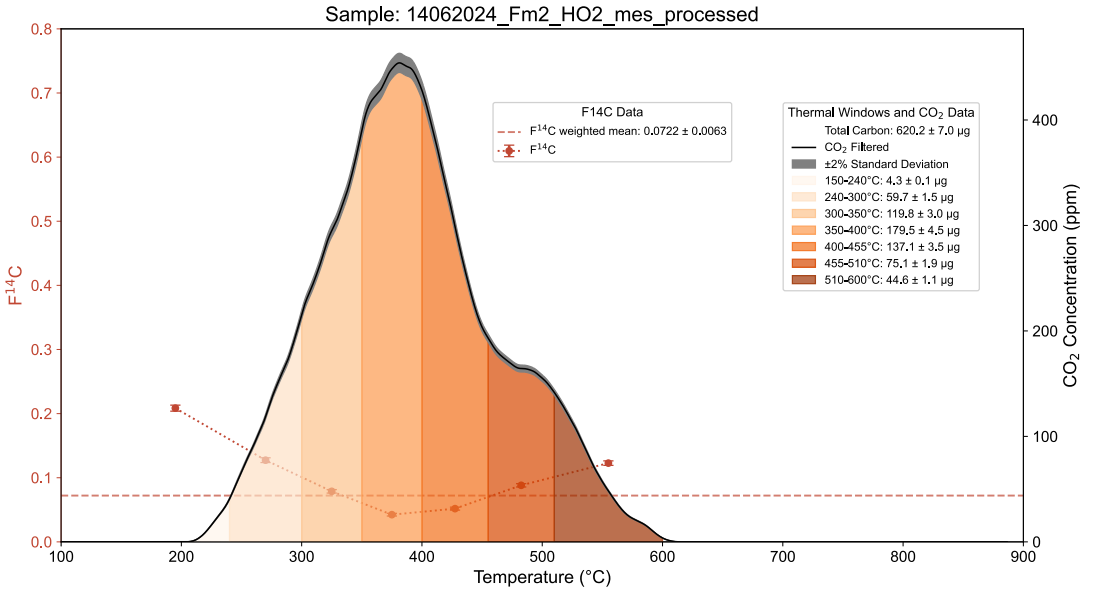

Figures S7. Thermogram of FM2-HO2 shows CO_2 release as a function of temperature for each sample, overlaid with corresponding $F^{14}C$ values across defined thermal windows. For each thermal window, the legends show the calculated carbon mass released (with associated error), the mass fraction (%), and the weighted $F^{14}C$ (with standard deviation). These data illustrate the relationship between carbon release dynamics, radiocarbon content, and the distribution of mass across the thermal profile.

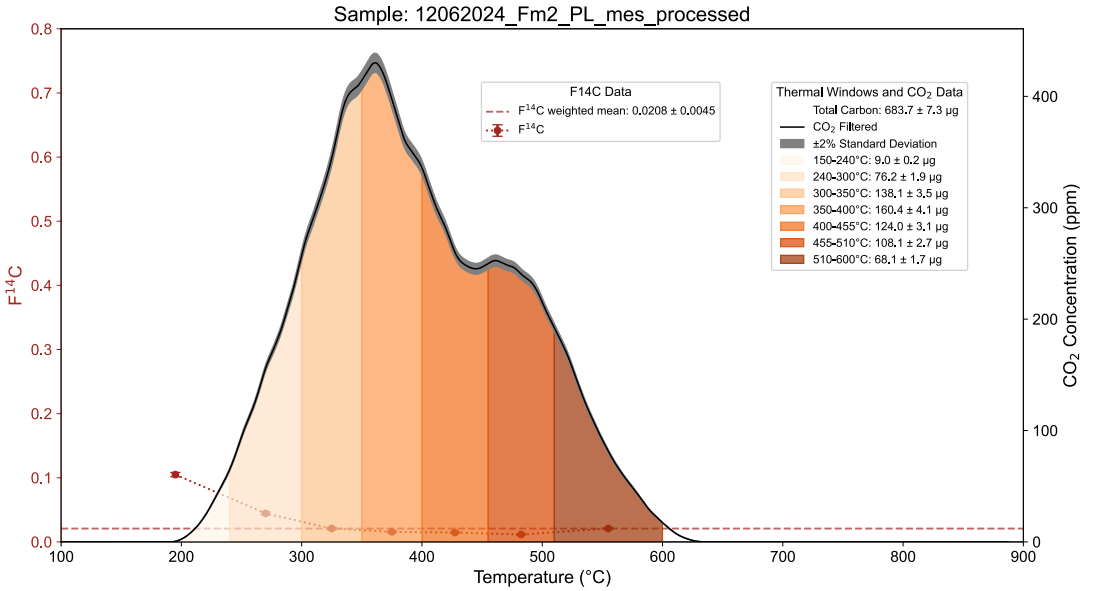

Figures S8. Thermogram of FM2-PL shows CO_2 release as a function of temperature for each sample, overlaid with corresponding $F^{14}C$ values across defined thermal windows. For each thermal window, the legends show the calculated carbon mass released (with associated error), the mass fraction (%), and the weighted $F^{14}C$ (with standard deviation). These data illustrate the relationship between carbon release dynamics, radiocarbon content, and the distribution of mass across the thermal profile.

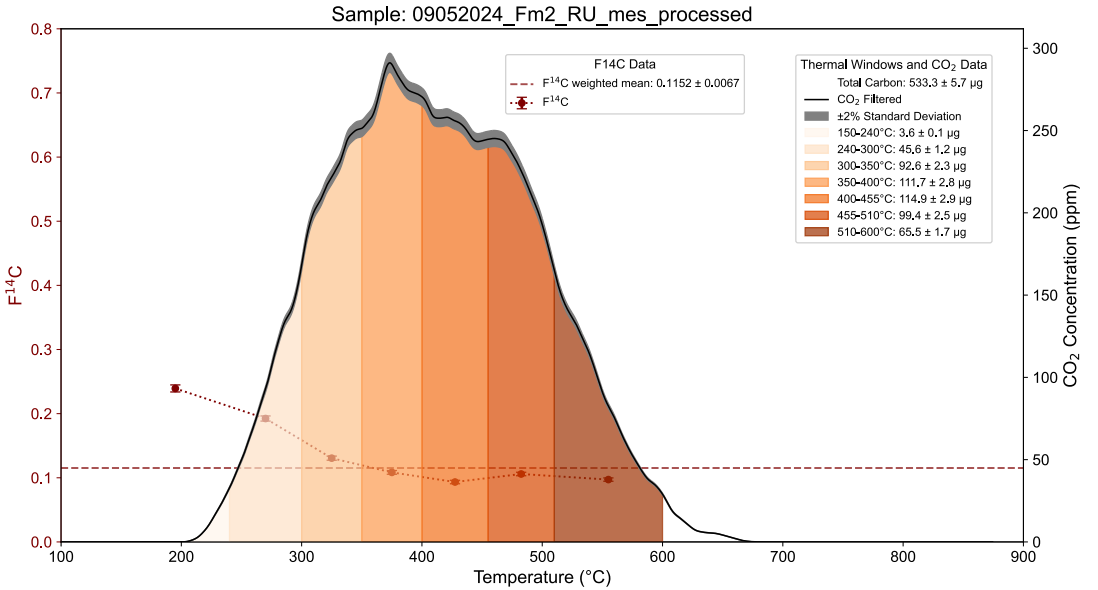

150 **Figures S9.** Thermogram of FM2-RU shows CO_2 release as a function of temperature for each sample, overlaid with corresponding $F^{14}C$ values across defined thermal windows. For each thermal window, the legends show the calculated carbon mass released (with associated error), the mass fraction (%), and the weighted $F^{14}C$ (with standard deviation). These data illustrate the relationship between carbon release dynamics, radiocarbon content, and the distribution of mass across the thermal profile.

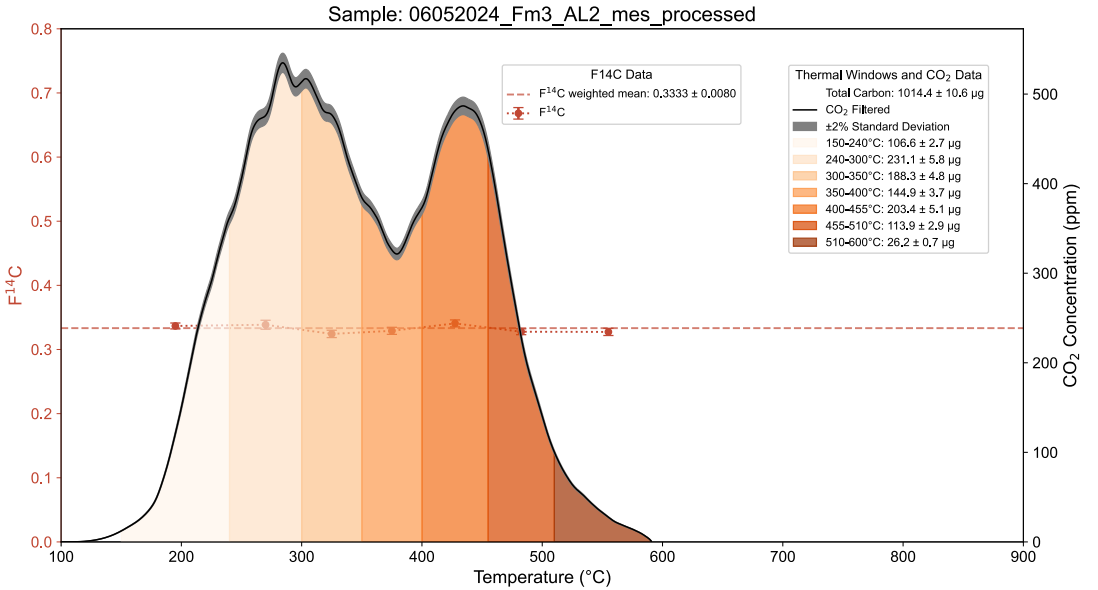

Figures S10. Thermogram of FM3-AL2 shows CO_2 release as a function of temperature for each sample, overlaid with corresponding $F^{14}C$ values across defined thermal windows. For each thermal window, the legends show the calculated carbon mass released (with associated error), the mass fraction (%), and the weighted $F^{14}C$ (with standard deviation). These data illustrate the relationship between carbon release dynamics, radiocarbon content, and the distribution of mass across the thermal profile.

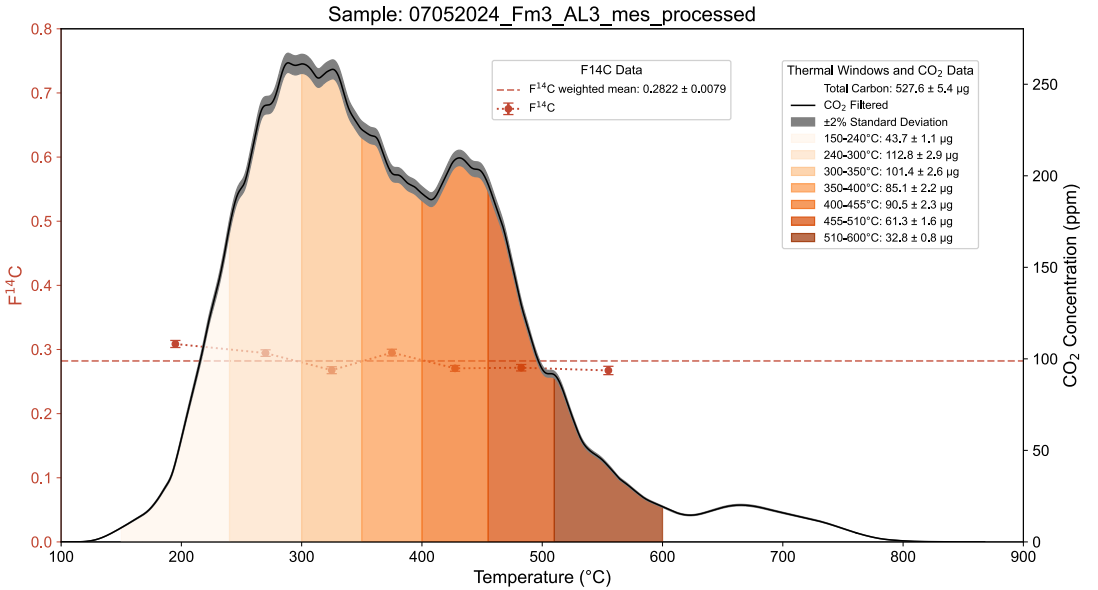

Figures S11. Thermogram of FM3-AL3 shows CO_2 release as a function of temperature for each sample, overlaid with corresponding $F^{14}C$ values across defined thermal windows. For each thermal window, the legends show the calculated carbon mass released (with associated error), the mass fraction (%), and the weighted $F^{14}C$ (with standard deviation). These data illustrate the relationship between carbon release dynamics, radiocarbon content, and the distribution of mass across the thermal profile.

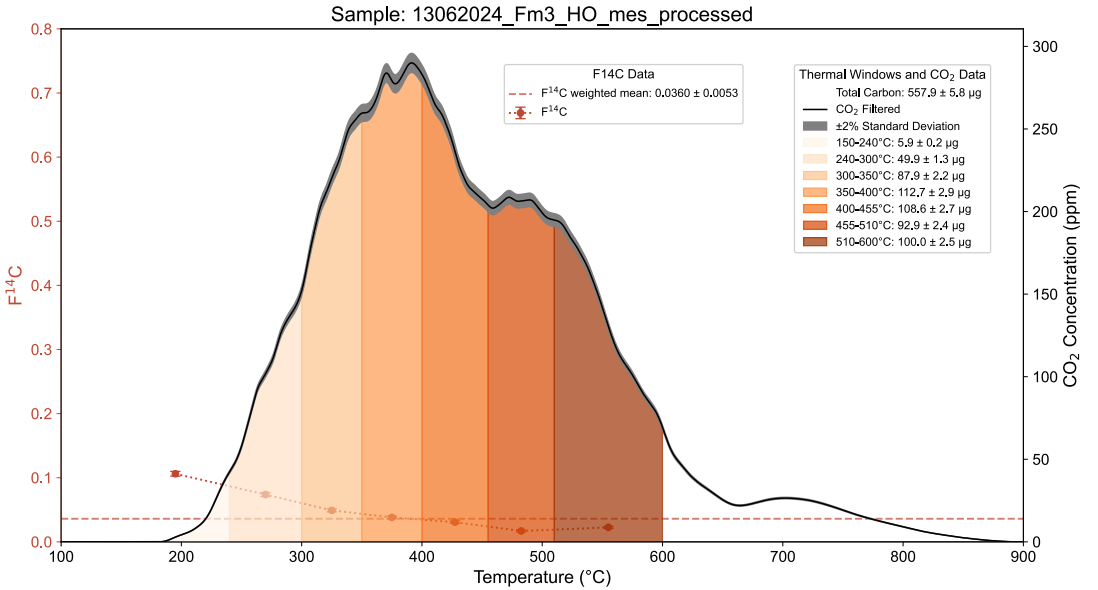

Figures S12. Thermogram of FM3-HO shows CO_2 release as a function of temperature for each sample, overlaid with corresponding $F^{14}C$ values across defined thermal windows. For each thermal window, the legends show the calculated carbon mass released (with associated error), the mass fraction (%), and the weighted $F^{14}C$ (with standard deviation). These data illustrate the relationship between carbon release dynamics, radiocarbon content, and the distribution of mass across the thermal profile.

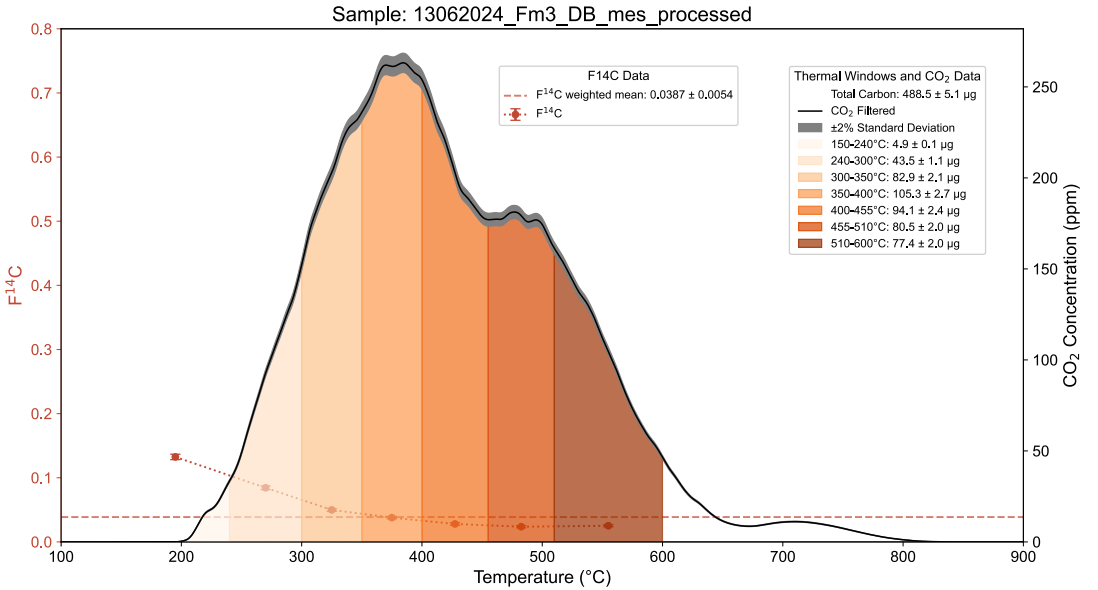

Figures S13. Thermogram of FM3-DB shows CO_2 release as a function of temperature for each sample, overlaid with corresponding $F^{14}C$ values across defined thermal windows. For each thermal window, the legends show the calculated carbon mass released (with associated error), the mass fraction (%), and the weighted $F^{14}C$ (with standard deviation). These data illustrate the relationship between carbon release dynamics, radiocarbon content, and the distribution of mass across the thermal profile.

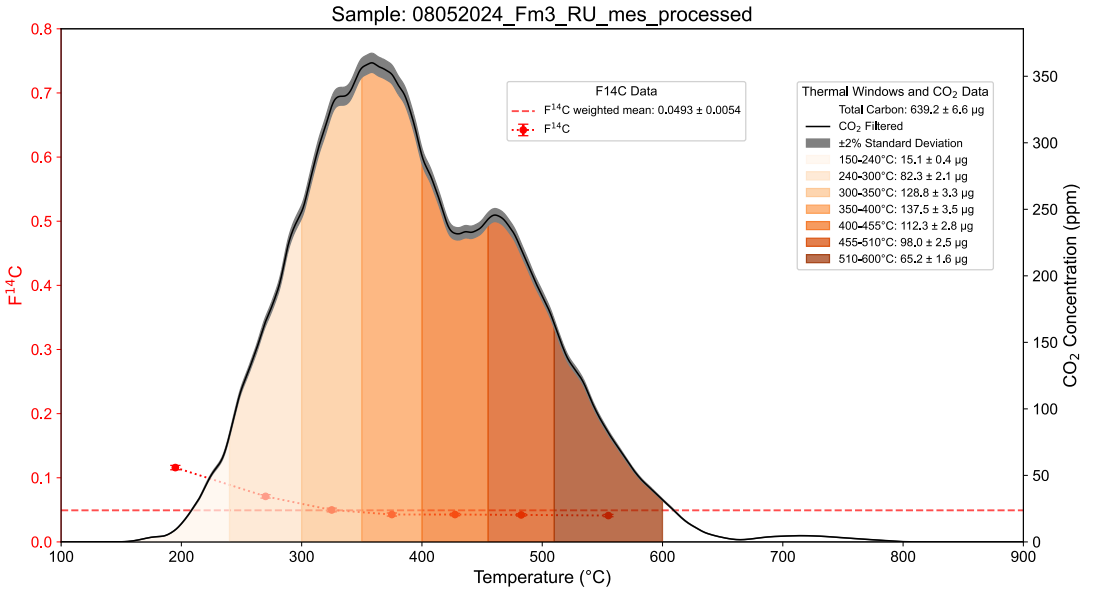

170 **Figures S14.** Thermogram of FM3-RU shows CO_2 release as a function of temperature for each sample, overlaid with corresponding $F^{14}C$ values across defined thermal windows. For each thermal window, the legends show the calculated carbon mass released (with associated error), the mass fraction (%), and the weighted $F^{14}C$ (with standard deviation). These data illustrate the relationship between carbon release dynamics, radiocarbon content, and the distribution of mass across the thermal profile.

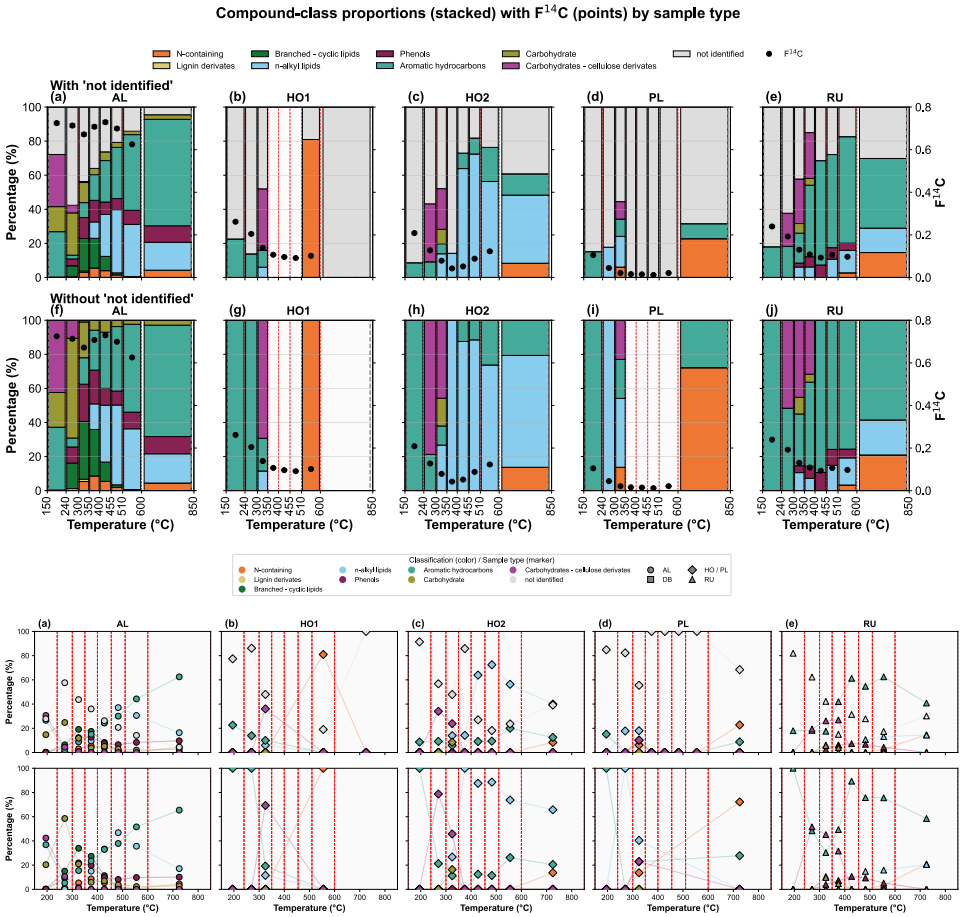

Figure S15. Normalised Ts-Py-GCMS peak-area distributions across thermal windows (150–850 °C) for Fm2 features. Top two rows (a–j): stacked plots showing compound-class distributions across thermal windows. Each feature is represented by paired panels — top includes all compounds; bottom excludes "not identified" compounds to emphasise major classes (N-containing, lignin derivatives, branched/cyclic lipids, n-alkyl lipids, phenols, aromatic hydrocarbons, carbohydrates, and cellulose derivatives). Feature–panel mapping: (a, f) active layer (AL); (b, g) Holocene permafrost shallow (HO1); (c, h)

Holocene permafrost deep (HO2); (d, i) Pleistocene layer (PL); (e, j) runoff (RU). Bottom two rows (a–e): scatter plots showing relative contributions of major compound classes versus thermal window for each geomorphic feature, highlighting contrasts in compound release, preservation, and compositional variability across Fm2.

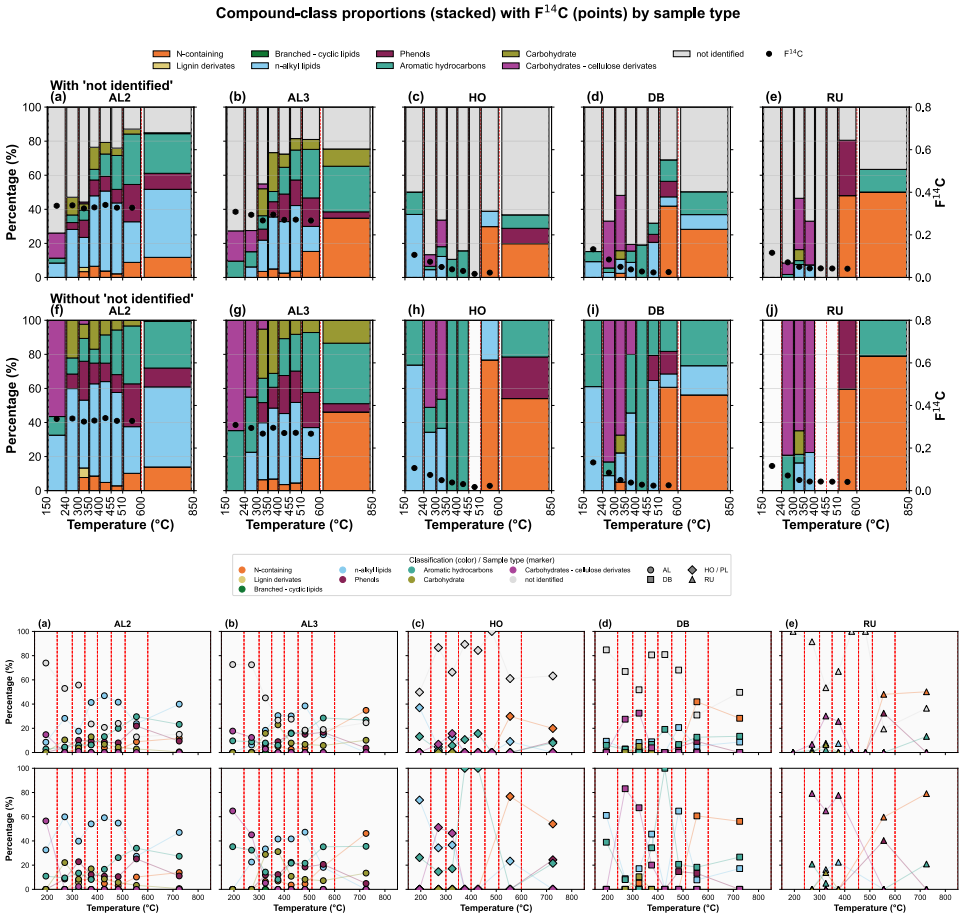

185

Figure S16. Normalised Ts-Py-GCMS peak-area distributions across thermal windows (150–850 °C) for Fm3 features. Top two rows (a–j): stacked plots showing compound-class distributions across thermal windows. Each feature is represented by paired panels — top includes all compounds; bottom excludes "not identified" compounds to emphasise major classes (N-containing, lignin derivatives, branched/cyclic lipids, n-alkyl lipids, phenols, aromatic hydrocarbons, carbohydrates, and cellulose derivatives). Feature–panel mapping: (a, f) shallow active layer (AL2), (b, g) deep active layer (AL3), (c, h) Holocene

permafrost (HO), (d, i) runoff (RU), (e, j) debris (DB). Bottom two rows (a–e): scatter plots showing relative contributions of major compound classes versus thermal window for each geomorphic feature, highlighting systematic compositional shifts with temperature and pronounced contrasts between shallow and deep active layers.

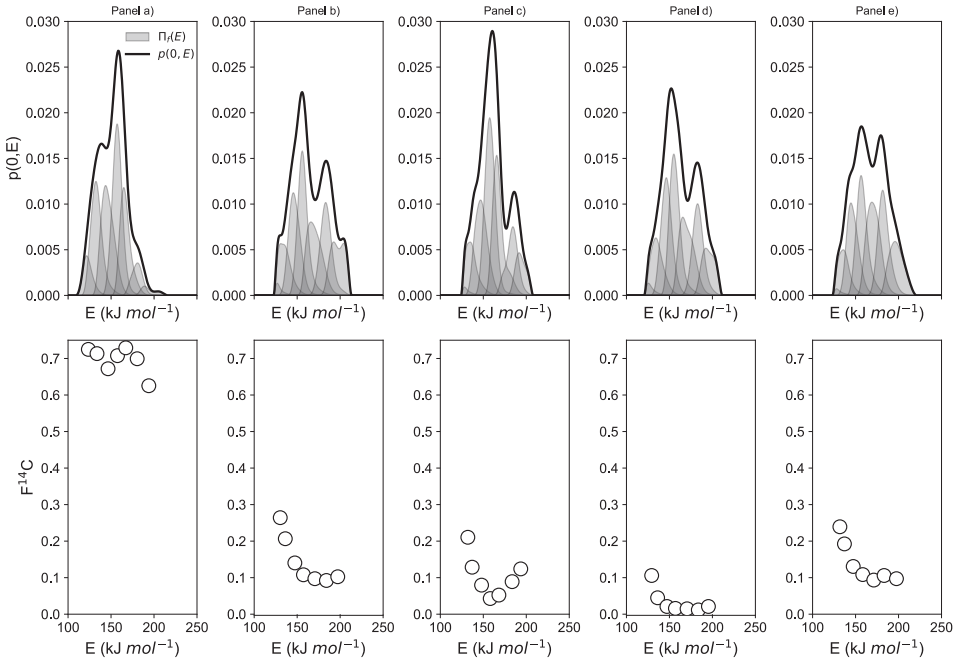

Figure S17. Energy distribution of organic matter thermal stability across geomorphic features at the Fm2 sit, following the energy model framework of Hemingway et al. (2019). Panels (a– e) show energy density profiles for: (a) active layer (AL), (b) and (c) Holocene permafrost (HO1, HO2), (d) Pleistocene permafrost (PL), and (e) runoff (RU). The top row displays energy distributions derived from ORO-AMS oxidation steps, while the bottom row overlays corresponding $F^{14}C$ values on the energy axis. This comparison highlights how carbon age aligns with thermal stability across geomorphic units.

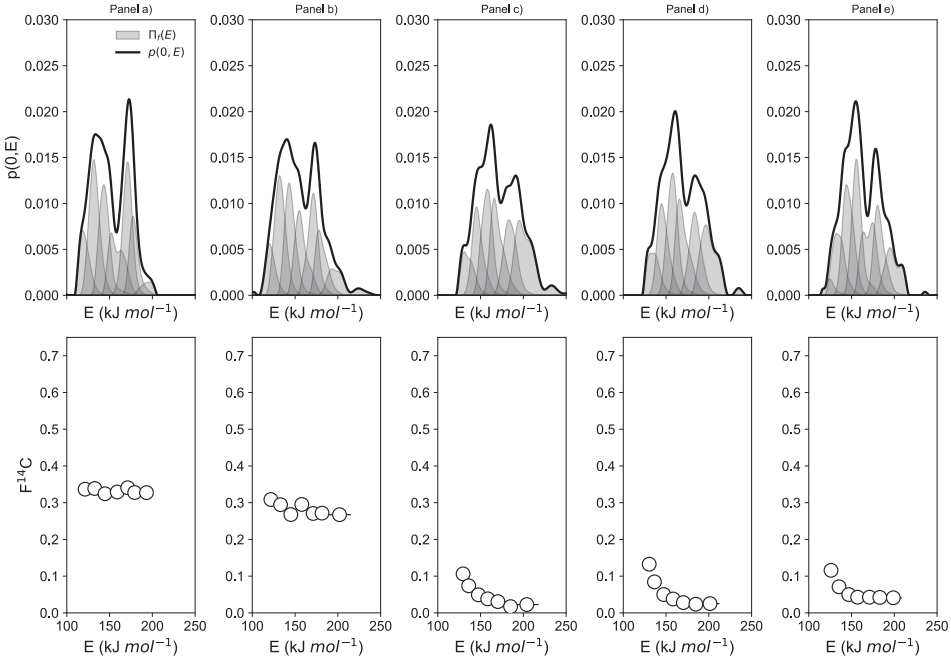

Figure S18. Energy distribution of organic matter thermal stability across geomorphic features at the Fm3 site, following the energy model framework of Hemingway et al. (2019). Panels (a)–(e) display the energy density profiles for: (a) active layer 2 (AL2), (b) active layer 3 (AL3), (c) Holocene permafrost (HO), (d) slump debris (DB), and (e) runoff (RU). The upper row presents energy distributions derived from ORO-AMS oxidation windows. The lower row overlays the corresponding $F^{14}C$ values on the same energy axis, illustrating the relationship between carbon age and energetic stability across compartments.

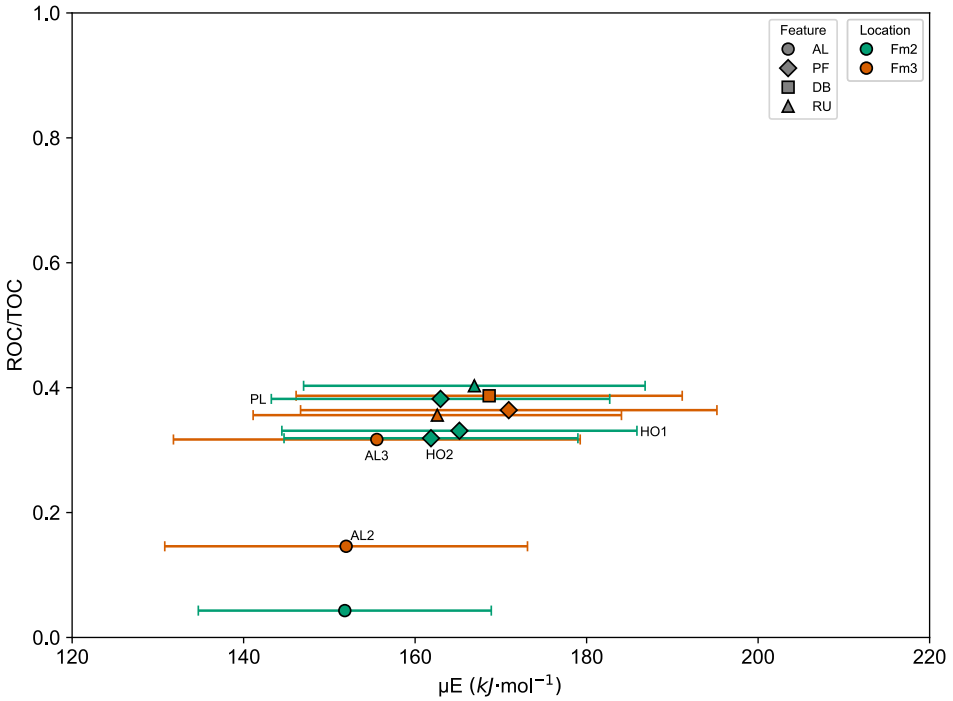

Figure S19. Cross-plot comparing the operationally defined recalcitrant-to-total organic carbon ratio (ROC/TOC) from ORO–AMS with mean activation energy (μE) derived from kinetic modelling. Error bars denote $\pm\sigma E$, representing standard deviations of activation-energy distributions. Samples from FM2 (green triangles) and FM3 (red circles) follow a coherent trend in which higher ROC/TOC values generally correspond to higher activation energies, indicating that thermally resistant carbon fractions are associated with more energetically stable material. Variation within each site reflects differences in organic-matter composition across geomorphic units (AL, PF, DB, RU).